AD-785 138

A LOW-SIDELOBE ANTENNA-RADOME STUDY AT K_a-BAND

Joseph T. Mayhan, et al

Massachusetts Institute of Technology

Prepared for:

Electronic Systems Division
Naval Electronic Systems Command

27 June 1974

DISTRIBUTED BY:

NTIS
National Technical Information Service
U. S. DEPARTMENT OF COMMERCE
5285 Port Royal Road, Springfield Va. 22151

UNCLASSIFIED

SECURITY CLASSIFICATION OF THIS PAGE (When Data Entered)

REPORT DOCUMENTATION PAGE		READ INSTRUCTIONS BEFORE COMPLETING FORM
1. REPORT NUMBER ESD-TR-74-227	2. GOVT ACCESSION NO.	3. RECIPIENT'S CATALOG NUMBER AD-785138
4. TITLE (and Subtitle) A Low-Sidelobe Antenna-Radome Study at K_a-Band		5. TYPE OF REPORT & PERIOD COVERED Technical Note
		6. PERFORMING ORG. REPORT NUMBER Technical Note 1974-35
7. AUTHOR(s) Mayhan, Joseph T. and Simmons, Alan J.		8. CONTRACT OR GRANT NUMBER(s) F19628-73-C-0002
9. PERFORMING ORGANIZATION NAME AND ADDRESS Lincoln Laboratory, M.I.T. P.O. Box 73 Lexington, MA 02173		10. PROGRAM ELEMENT, PROJECT, TASK AREA & WORK UNIT NUMBERS Project No. 1508A
11. CONTROLLING OFFICE NAME AND ADDRESS Naval Electronic Systems Command Department of the Navy Washington, DC 20360		12. REPORT DATE 27 June 1974
		13. NUMBER OF PAGES 74
14. MONITORING AGENCY NAME & ADDRESS (if different from Controlling Office) Electronic Systems Division Hanscom Air Force Base Bedford, MA 01730		15. SECURITY CLASS. (of this report) Unclassified
		15a. DECLASSIFICATION DOWNGRADING SCHEDULE

16. DISTRIBUTION STATEMENT (of this Report)

Approved for public release; distribution unlimited.

17. DISTRIBUTION STATEMENT (of the abstract entered in Block 20, if different from Report)

18. SUPPLEMENTARY NOTES

None

19. KEY WORDS (Continue on reverse side if necessary and identify by block number)

low-sidelobe antenna	satellite communications	lens antennas
radomes	Navy communications	dish antennas

20. ABSTRACT (Continue on reverse side if necessary and identify by block number)

This technical report summarizes the results of extensive measurements designed to evaluate the effects of a homogeneous, spherical, glass (Pyrex) radome on the sidelobe structure of an isolated, low-sidelobe antenna. The antenna-radome combination is intended for use on a submarine for satellite communication. The results are divided into three basic categories: first, the performance of an optimum low-sidelobe antenna is discussed; second, the measured and calculated performance of various candidate antennas without radome will be presented; finally, the effects of the spherical radome on the radiation patterns of the isolated antennas will be considered. Both lens and paraboloidal dish antennas are considered. The results of the measurements show that with the lens-radome combination low sidelobes can be achieved, whereas the dish-radome design presents considerable difficulties in achieving a low-sidelobe pattern.

DD FORM 1473 1 JAN 73 EDITION OF 1 NOV 65 IS OBSOLETE

UNCLASSIFIED

SECURITY CLASSIFICATION OF THIS PAGE (When Data Entered)

MASSACHUSETTS INSTITUTE OF TECHNOLOGY
LINCOLN LABORATORY

A LOW-SIDELOBE ANTENNA-RADOME STUDY AT K_a-BAND

J. T. MAYHAN
A. J. SIMMONS

Group 61

TECHNICAL NOTE 1974-35

27 JUNE 1974

LEXINGTON MASSACHUSETTS

ABSTRACT

This technical report summarizes the results of extensive measurements designed to evaluate the effects of a homogeneous, spherical, glass (Pyrex) radome on the sidelobe structure of an isolated, low-sidelobe antenna. The antenna-radome combination is intended for use on a submarine for satellite communication. The results are divided into three basic categories: first, the performance of an optimum low-sidelobe antenna is discussed; second, the measured and calculated performance of various candidate antennas without radome will be presented; finally, the effects of the spherical radome on the radiation patterns of the isolated antennas will be considered. Both lens and paraboloidal dish antennas are considered. The results of the measurements show that with the lens-radome combination low sidelobes can be achieved, whereas the dish-radome design presents considerable difficulties in achieving a low-sidelobe pattern.

A Low-Sidelobe Antenna-Radome Study
at K_a-Band

I. Characterization of the Ideal, Low-Sidelobe Radiation Pattern

In order to evaluate the feasibility of designing an antenna having specific size, gain and sidelobe requirements, it is necessary to specify an unambiguous set of criteria which define what one might refer to as characterizing the "optimum antenna." Then one can readily evaluate how well a specific antenna performs relative to these criteria, and a basis for comparisons between several candidate antennas is established. The specific requirements for the antenna-radome combination under consideration stem from its potential use on a submarine for surface to satellite communication. Thus the radome must be structurally strong, requiring a radome several wavelengths thick at the frequency of interest (37 GHz). The composite antenna-radome structure must occupy minimum volume, but is required to have maximum gain and minimum possible sidelobe level. The radome itself must offer negligible pattern distortion with look angle, which scans the entire upper hemisphere above the surface. This leads to the obvious choice of a spherical radome, to be considered here, although other shapes are presently under consideration. The sidelobe requirement has been set at nominally 40-dB first sidelobe. However, specifying only the level of the first sidelobe and not its position is a rather vague specification and can lead to a non optimum design. To demonstrate this, Fig. 1 illustrates the radiation patterns of an 18-inch circular aperture having two different aperture distributions designed for low sidelobes. One has a 24-dB edge taper yielding a 40-dB first sidelobe and the other a 40-dB edge taper producing a 55-dB first sidelobe.

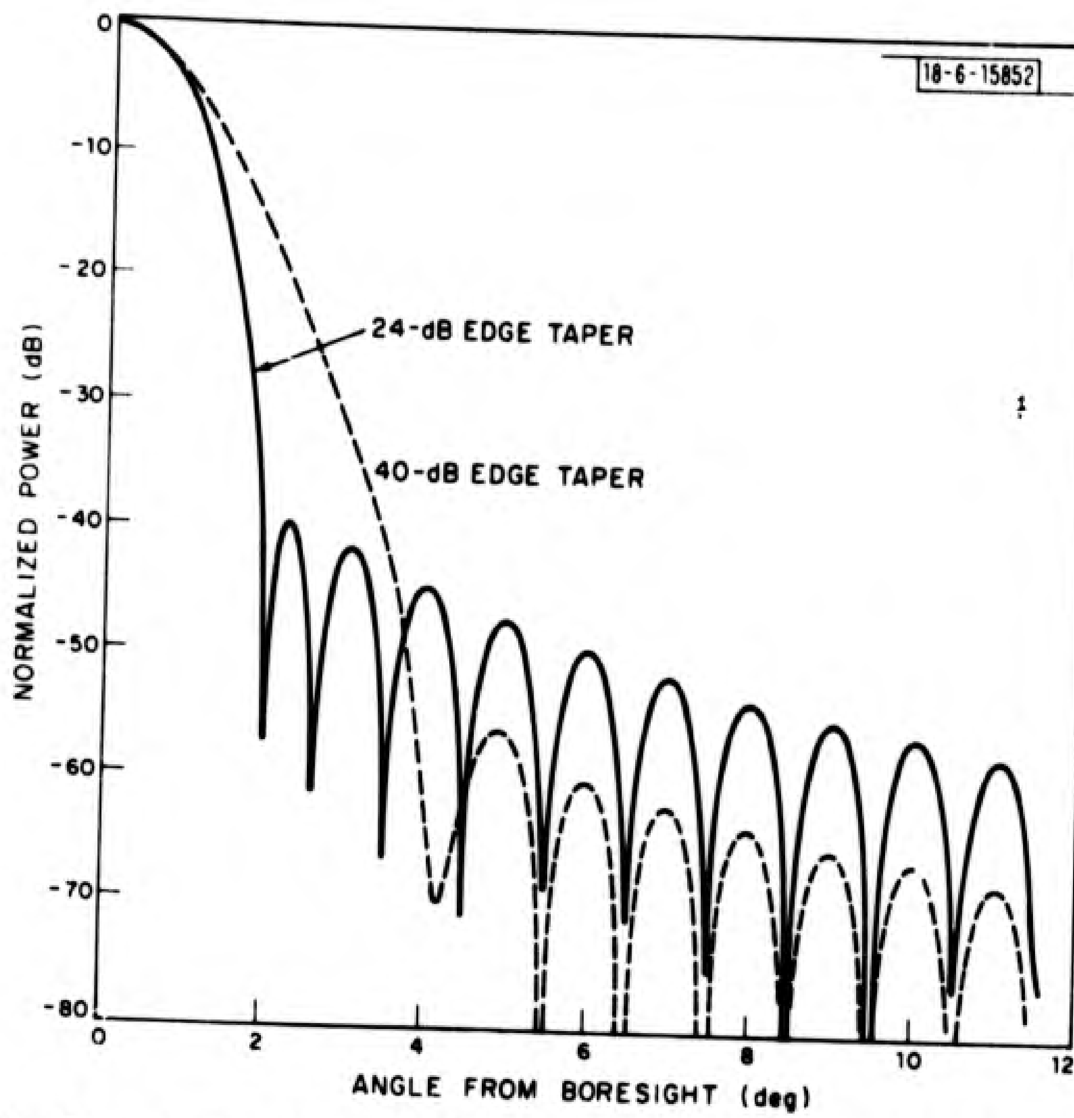

Fig. 1. Comparison of two-low-sidelobe patterns, 18-inch aperture, f = 37 GHz.

Clearly, the pattern with the higher first sidelobe is more suitable for minimum detectability for angles outside 2^o. Thus it becomes clear that, along with specifying the maximum allowable field in the sidelobe region, one must also specify a critical solid angle outside which the field cannot rise above this level. With this in mind we define the ideal pattern as follows:

> "For a fixed aperture size, the ideal pattern is that pattern which maximizes the directivity on boresight, subject to the constraint that the field outside a specified conical solid angle Ω_c about boresight is less than 40 dB."

The aperture distribution which produces this radiation pattern is not rigorously known, but if one relaxes the directivity condition and replaces the condition on maximum directivity with a condition which minimizes the beamwidth, the ideal pattern is then readily determined to be a Taylor pattern,[1] which gives the optimum tradeoff between beamwidth and sidelobe level. The ideal Taylor pattern is characterized by a single main beam, followed by uniform sidelobes. This pattern is, of course, physically unrealizable, but can be approximated closely if the sidelobes are allowed to decay after the first few lobes occur. The Taylor radiation pattern is circularly symmetric about boresight and hence only the cone angle θ_c relative to boresight need be specified.

It is interesting to compare how the critical angle θ_c changes as a function of aperture size. To examine this, consider the ideal Taylor far-field power pattern

$$\cosh^2(u^2 - A^2)^{1/2} \tag{1}$$

where cosh A is the sidelobe level, $u = (kD/2)\sin\theta$, $k = 2\pi/\lambda$, λ = signal wavelength, θ = pattern angle about boresight and D = aperture diameter. If we specify the angle θ_c via the position of the first null, i.e.,

$$\sqrt{u_c^2 - A^2} = \pi/2 \tag{2}$$

where $u_c = (\frac{kD}{2}) \sin\theta_c$, then it is readily shown that for 40-dB sidelobes,

$$D = \frac{2u_c}{k\sin\theta_c} \tag{3}$$

Choosing f = 37 GHz we obtain

$$D \approx .56/\sin\theta_c \tag{4}$$

Thus using the ideal Taylor pattern as the measure of the optimum pattern, Eq. (4) specifies the MINIMUM size aperture needed to obtain a radiation pattern below 40 dB for $\theta > \theta_c$. Figure 2 illustrates the angle θ_c as a function of aperture size at f = 37 GHz. Hence for an 18-inch aperture the very best one could hope to achieve would be to constrain the power level to below 40 dB outside a conical angle of 1.8° about boresight. If the aperture size is reduced to 10 inches, the critical angle increases to 3.2°. From the curve one observes that an 18-inch aperture represents, from a practical viewpoint, the diameter giving maximum use of the aperture, since any increase in aperture size would yield only slight benefit in decreasing θ_c. At the lower end of the curve the critical angle decreases very rapidly with increase in aperture size, and the benefits of increasing the aperture size even slightly are

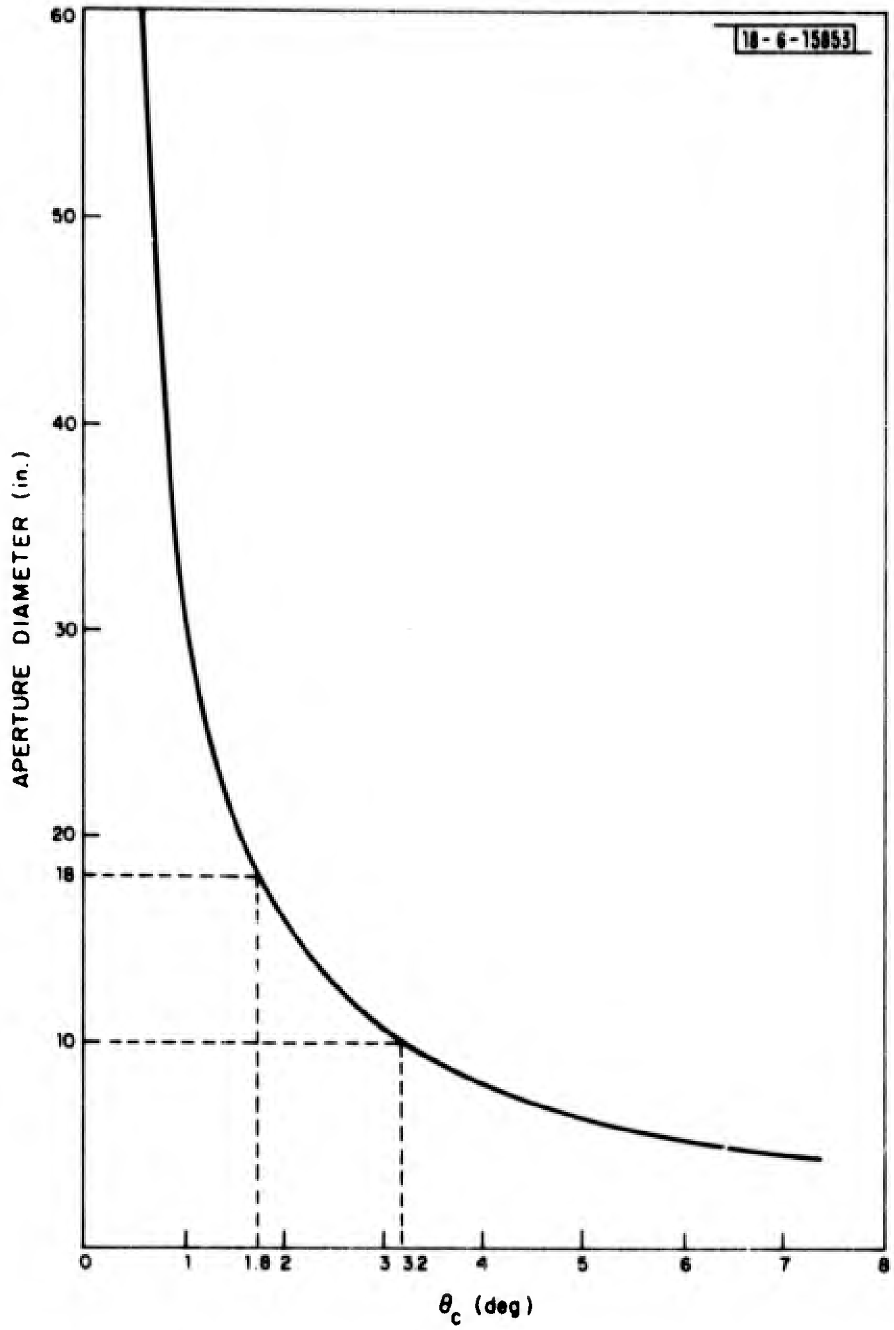

Fig. 2. Minimum aperture size required for pattern <40 dB for $\theta > \theta_c$, f = 37 GHz.

readily apparent. One suspects that the reason the optimum size appears to be near 18 inches is that the gain of such an aperture is about 40 dB, so that the specified sidelobe level, -40 dB, is near the isotropic level. Clearly, another choice of desired sidelobe level would lead to a different optimum diameter. Of course these are very ideal results, for with any high-frequency aperture-type antenna one cannot precisely control the taper near the edge of the aperture. Thus the curve in Fig. 2 applied to a practical antenna system would be displaced somewhat to the right, particularly for smaller aperture diameters.

In Fig. 3 we illustrate the aperture distribution which produces the optimum pattern for an 18-inch aperture at 37 GHz, and in Fig. 4 the corresponding radiation pattern. Observe that the position of the first null occurs at $\theta_c \approx 1.8°$, consistent with the results of Fig. 2. The aperture taper was obtained using the tables in Hansen,[2] which give the aperture distribution producing a Taylor pattern for fixed sidelobe level. The resultant patterns were then computed using the formulation developed in Appendix II.

II. Isolated Antenna Study

In order to determine how closely one can approach the ideal criteria discussed in Section I, tests were performed on four separate candidate antennas. The aperture diameter of each was fixed in the range (18-20) inches at a frequency of 37 GHz. The various candidate antennas are briefly described below:

TEST ANTENNAS

1. 18" plano-convex lens. Focal length = 21". Conical, corrugated feed horn. Lens obtained on loan from Rome Air Development Center (see Fig. 5).

2. 18" plano-convex lens. Focal length = 15". Conical, corrugated feed horn. Lens scaled to V-band (61 GHz) (see Fig. 9).

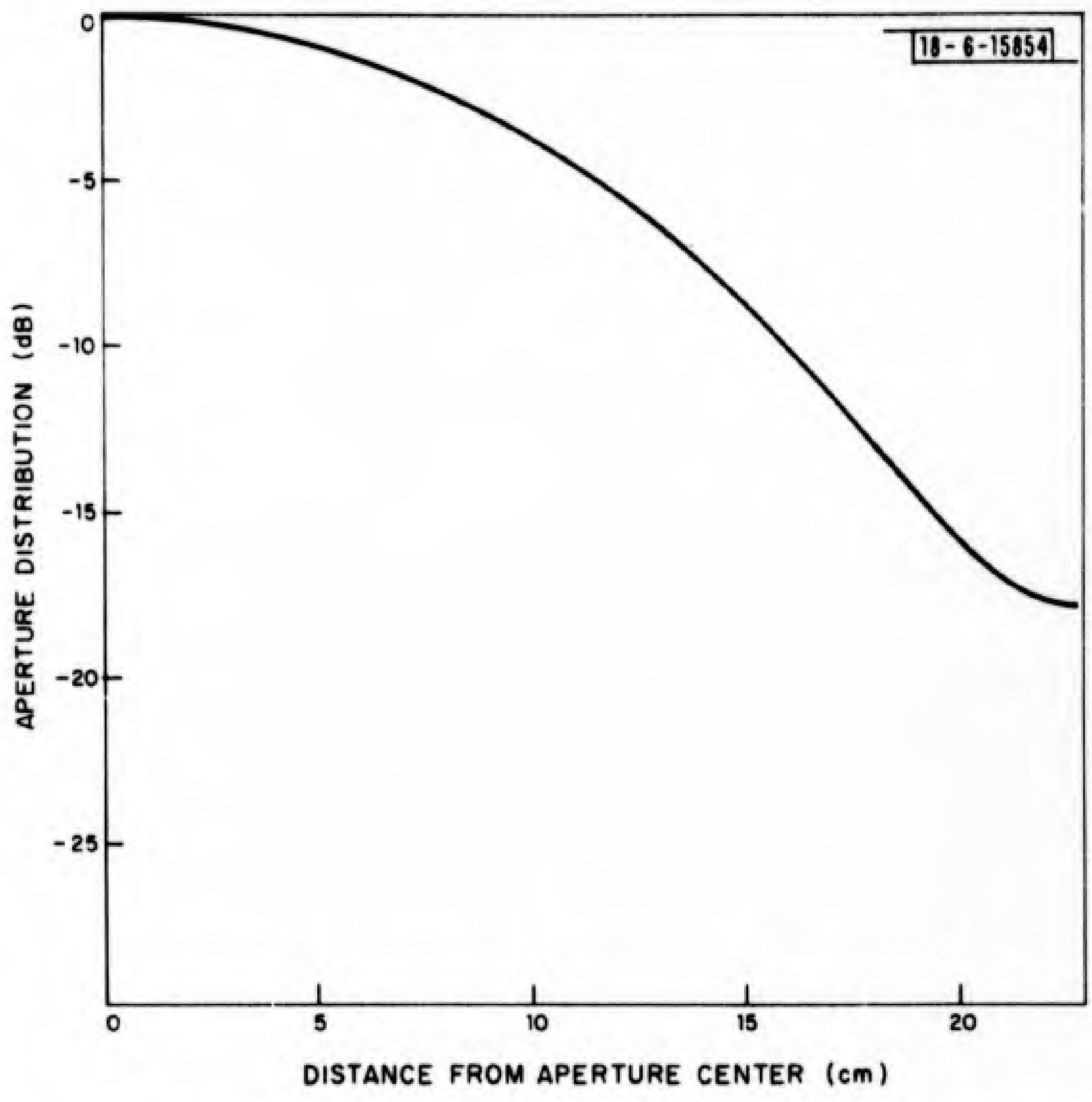

Fig. 3. Optimum 40 dB sidelobe aperture distribution. 18-inch aperture distribution, 18-inch aperture, f = 37 GHz.

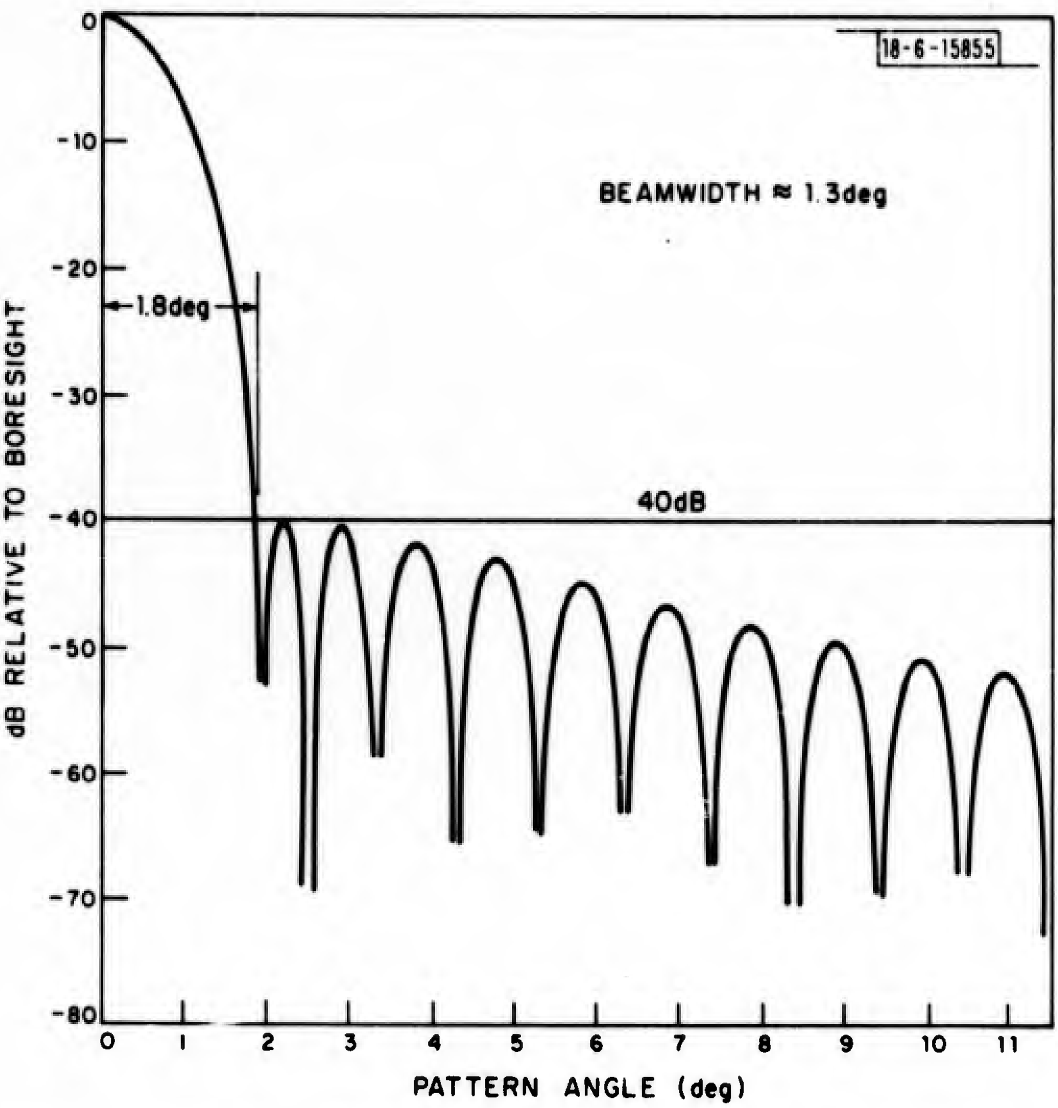

Fig. 4. Optimum radiation pattern, 18-inch aperture, f = 37 GHz.

3) 20" parabolic dish. Waveguide feed crossing over the rim in the H-plane. Scaled to V-band.

4) 20" parabolic dish. Axially symmetric corrugated cup, rear feed. Scaled to V-band (see Fig. 15).

The 18-inch plano-convex lens with 21-inch focal length obtained from Rome Air Development Center will be referred to as the RADC lens. The remaining lens and dishes were designed as part of a combination antenna-radome experimental setup to determine the effects on the radiation pattern of the isolated antennas when enclosed by a spherical radome enclosure. The 18-inch plano-convex lens type was selected following an extensive study of various possible lens geometries which might be used. The details of the lens design are presented in Appendix I. The 20-inch parabolic dish was a commercially available TRG dish, slightly modified so that the over-the-rim feed would fit compactly inside the radome. The same dish was then modified and used with an axially symmetric feed design using a corrugated cup, rear feed. In order to facilitate the construction of a reasonable size radome, the entire measurement was scaled to 61 GHz. The effects of the radome on the radiation patterns will be discussed in Section III, and only the isolated antennas are considered here.

A. RADC Lens

A conical, corrugated feed horn was designed for use with the RADC lens. The horn has a edge taper of approximately 18 dB, and the feed and lens were mounted as illustrated in Fig. 5. Using the measured feed patterns, the aperture distribution outside the lens was determined and is illustrated in Fig. 6. The E- and H-plane patterns differed very little and so the average

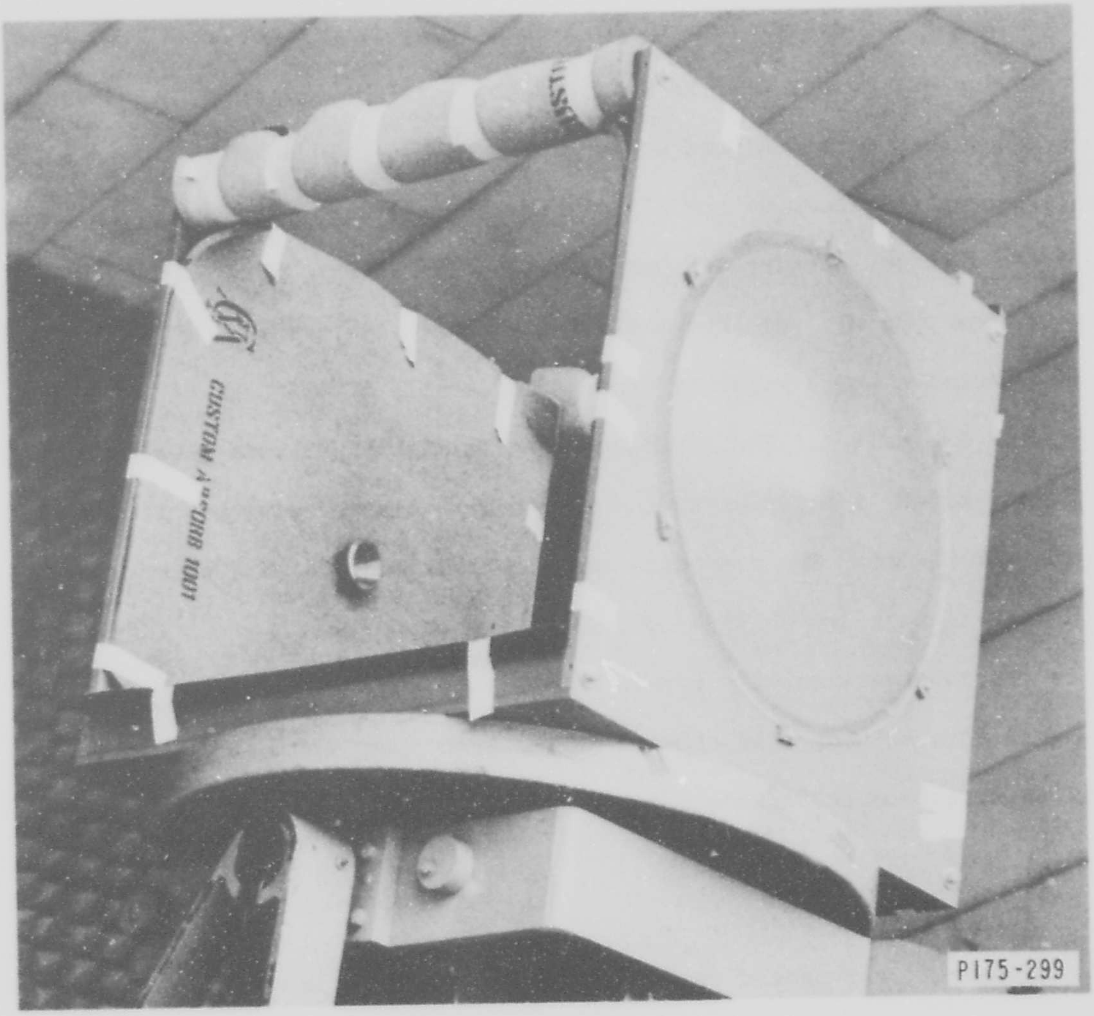

Fig. 5. RADC lens and feed.

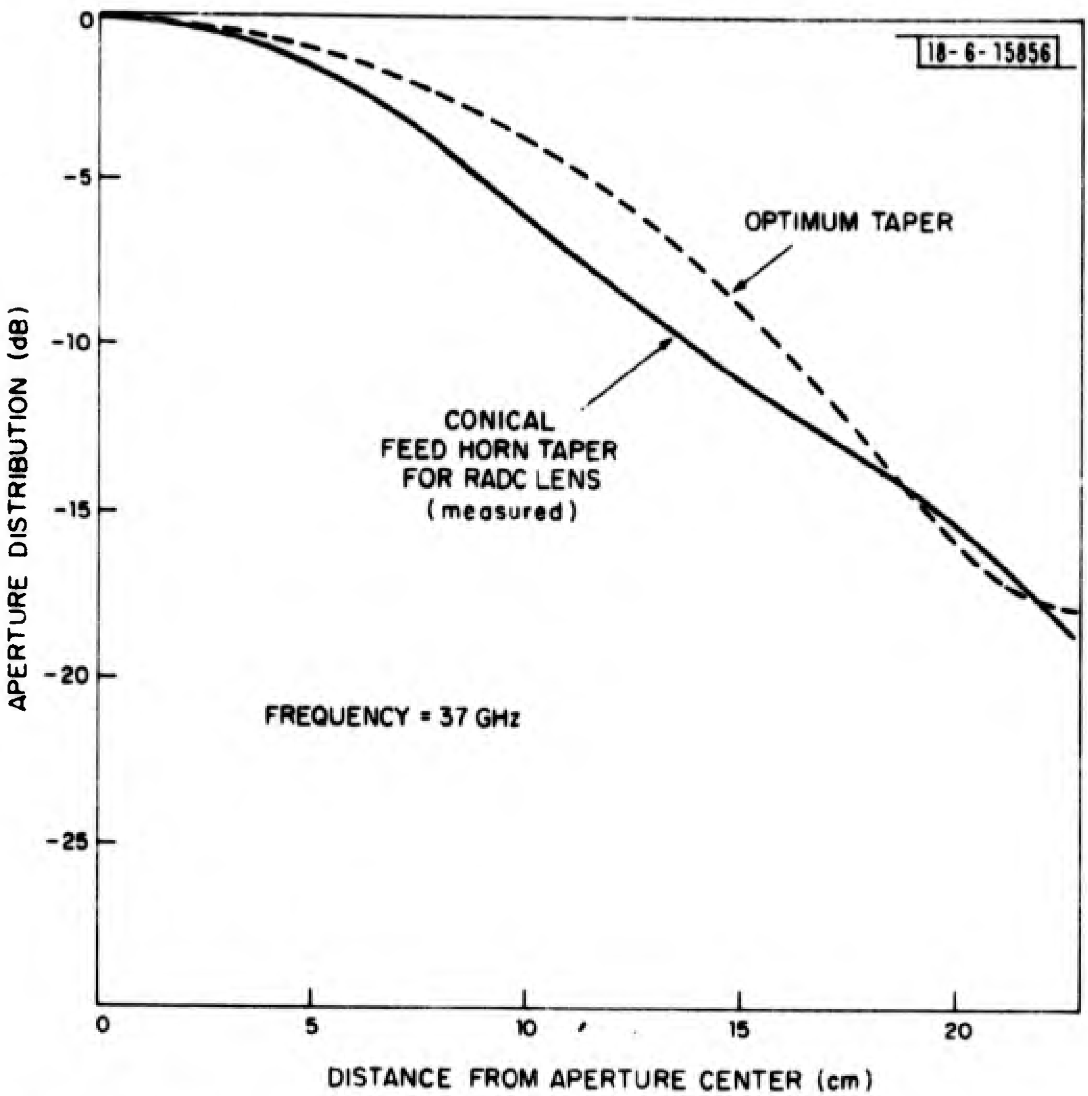

Fig. 6. Aperture distribution for RADC lens compared to optimum.

of the E- and H-plane feed patterns was used. The effect the lens introduces on the taper, as shown in Appendix I, is quite small, and was found to have a negligible effect on the radiation pattern. Thus it was omitted in the numerical calculations. For comparison the aperture distribution corresponding to the optimum radiation pattern is also sketched in Fig. 6. Although the edge taper is of the correct magnitude, the feed distribution is somewhat lower than optimum over the inner portion of the aperture, leading to a smaller effective diameter. Thus we expect a somewhat broader pattern with slightly increased sidelobes. The measured and computed radiation patterns are illustrated in Figs. 7 and 8. The computed patterns were obtained using the formulation in Appendix II. The measured patterns yield a critical angle $\theta_c \approx 4.2°$ which agrees with the computed value of 4.2°. A contour plot of the complete pattern verified this value of θ_c in all planes.

B. V-Band Scaled Lens--Experimental Results

The next three candidate antennas were part of the dish and lens radome study to determine the effects introduced by a spherical radome enclosure on the radiation pattern. The desired lens at 37 GHz was an 18-inch plano-convex lens with a focal length of 15 inches, which scale to roughly 10 inches and 9.1 inches, respectively, at 61 GHz. Several different conical feed horns were fabricated and the taper most closely approximating the optimum is considered here. The lens and feed were mounted in the cylindrical chamber as shown in Fig. 9. The mount was designed for use in the radome experiment to be described later. The measured E- and H-plane feed horn patterns were used to determine the aperture distribution shown in Fig. 10, where the optimum

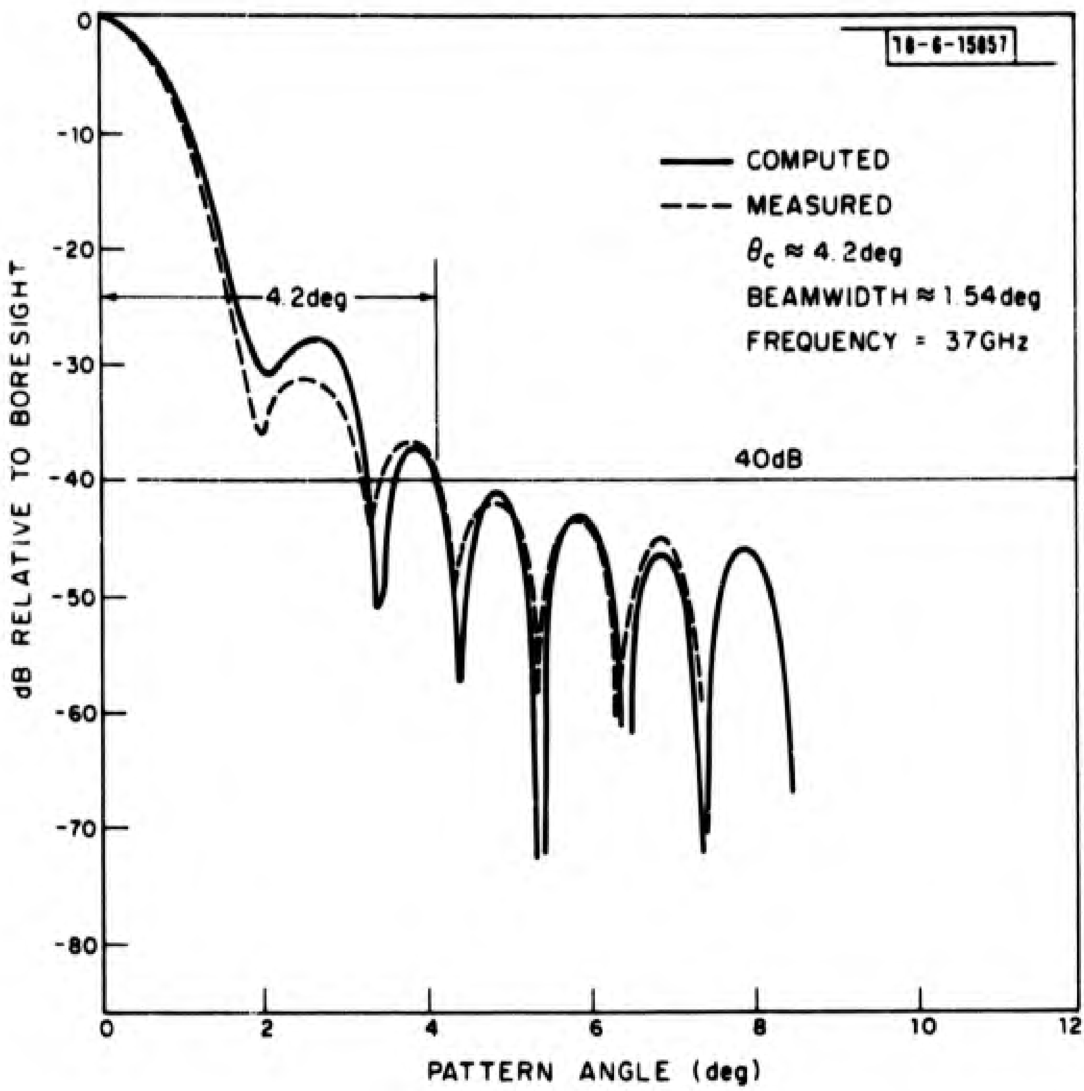

Fig. 7. E-plane measured and computed radiation patterns for RADC lens.

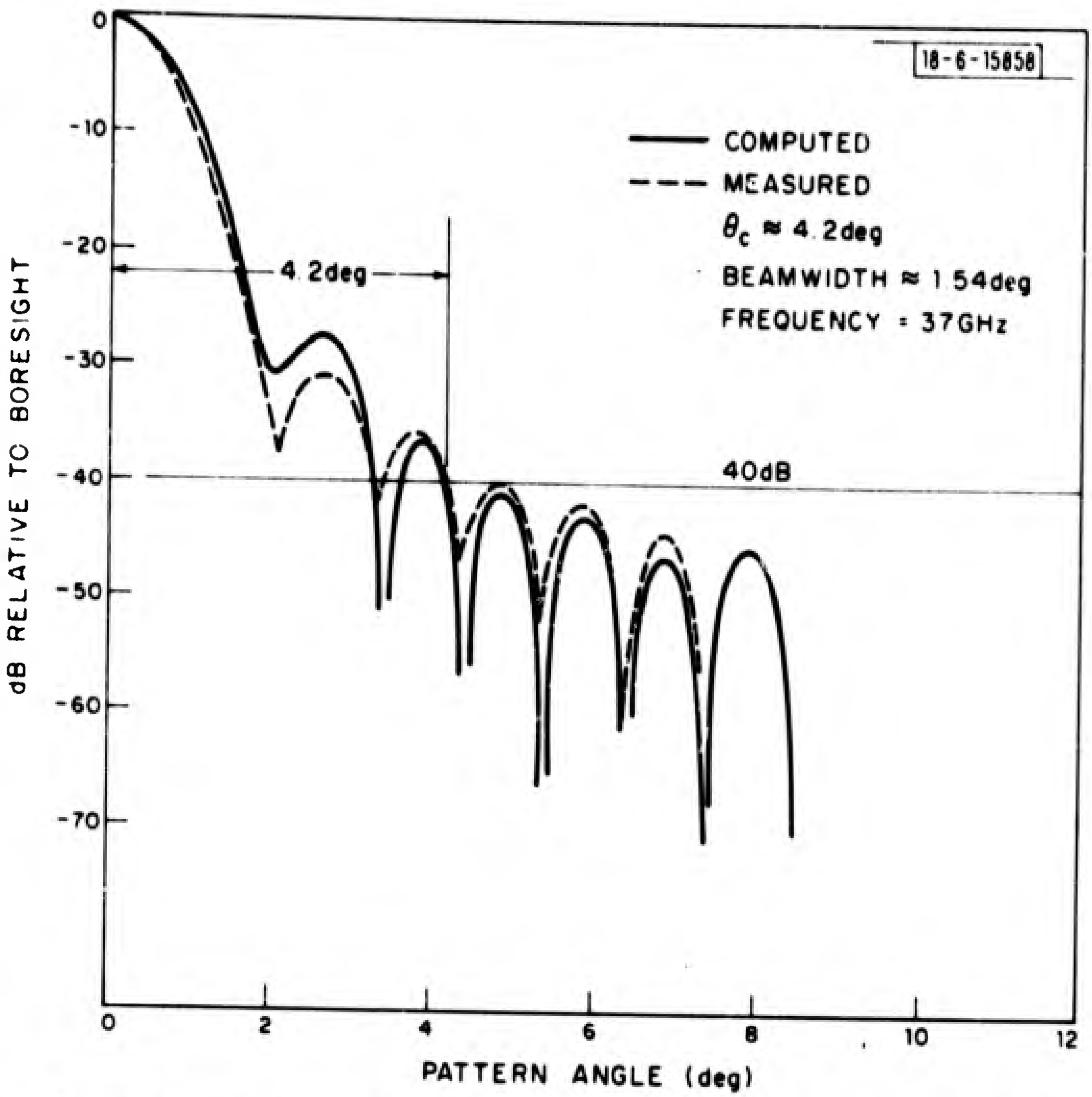

Fig. 8. H-plane measured and computed radiation patterns for RACD lens.

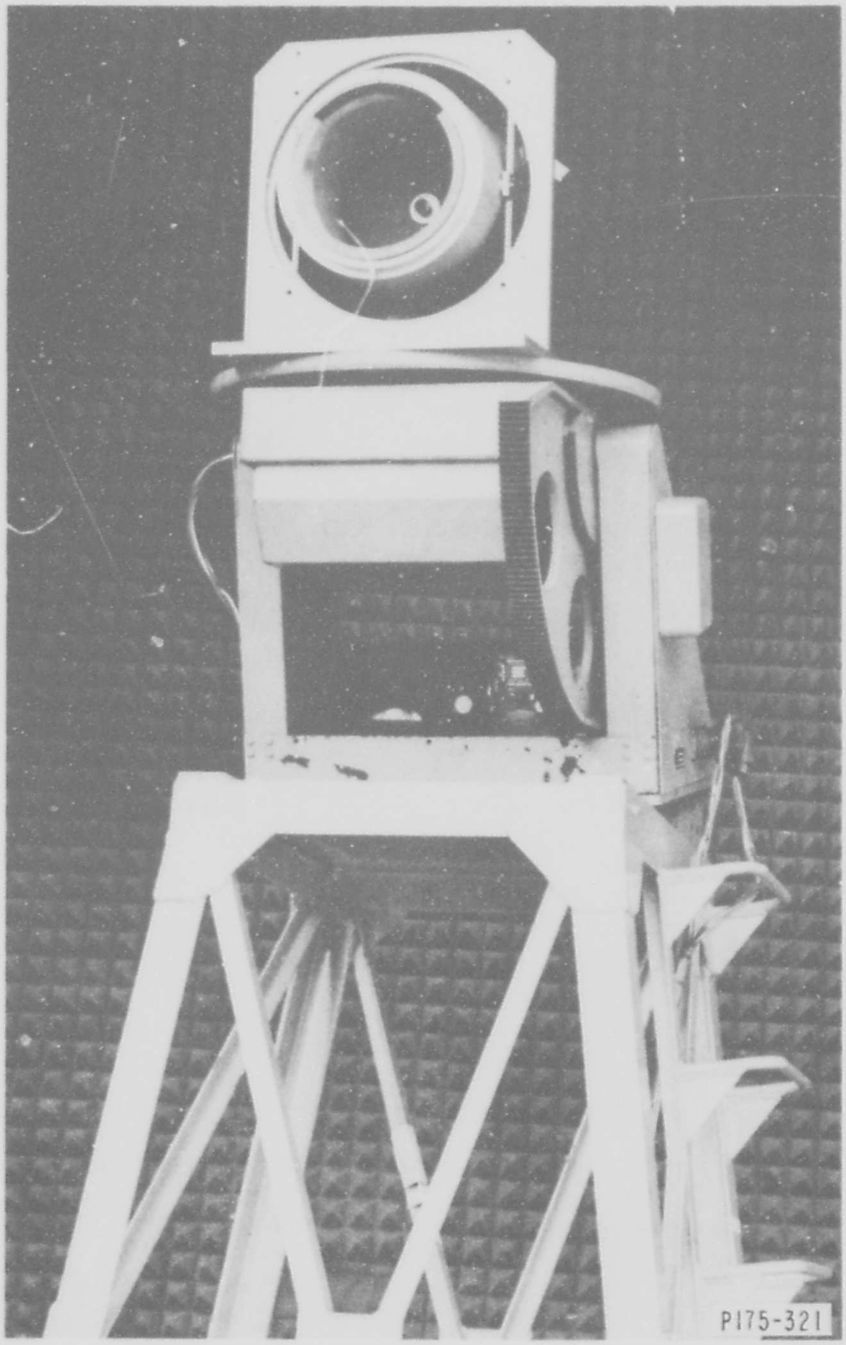

Fig. 9. V-Band lens experimental setup.

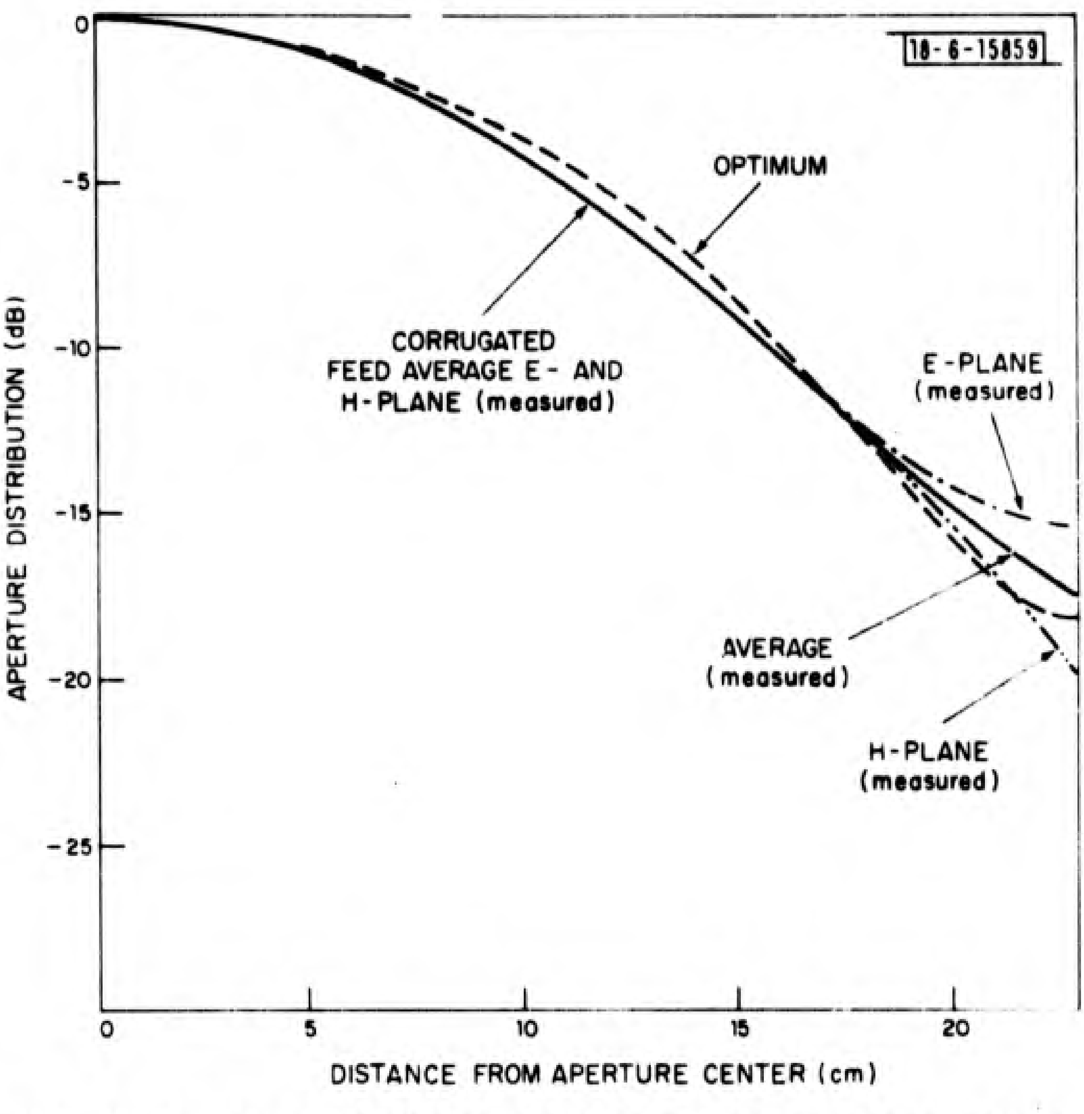

Fig. 10. Aperture distribution for V-Band lens compared to optimum.

taper is also shown. The feed patterns were somewhat unequal at the outer portion of the lens, resulting in an E-plane aperture distribution considerably higher than the H-plane distribution at the outer edge. The average edge taper is higher than optimum and the distribution over the aperture center is somewhat lower than optimum, again resulting in higher sidelobes and wider null positions when compared to the optimum pattern. The corresponding E- and H-plane measured and computed patterns are shown in Fig. 11. The patterns were computed using the average of the E- and H-plane aperture distributions. As expected the beamwidth is narrower than that for the RADC lens, but the measured patterns are somewhat high in the near-in sidelobe region, and the critical angle is essentially the same as the RADC lens at 4.25°, but is greater than the computed value of 4.1°. The H-plane pattern has considerably lower near in sidelobes, which would be expected as the H-plane aperture distribution corresponds more closely to the optimum taper. Gain measurements set the gain at approximately 40.5 dB.

C. V-Band Feed Modified--Experimental Results

Upon comparison of the optimum and measured aperture distributions for the V-band feed just discussed, it is readily seen that the central distribution closely approximates the optimum, but the E-plane edge taper is much too high. In order to compensate for this and lower the edge taper, a piece of absorber was shaped into a conical form and inserted between the feed horn and outer edge of the lens as shown in Fig. 12. The idea here is that a wave launched along the absorber would be slightly attenuated at the outer edge of the lens, thus reducing the edge taper, but the taper in towards the aperture center would be unaffected. This would also result in a somewhat lower H-plane taper, but calculations indicated that this would not sig-

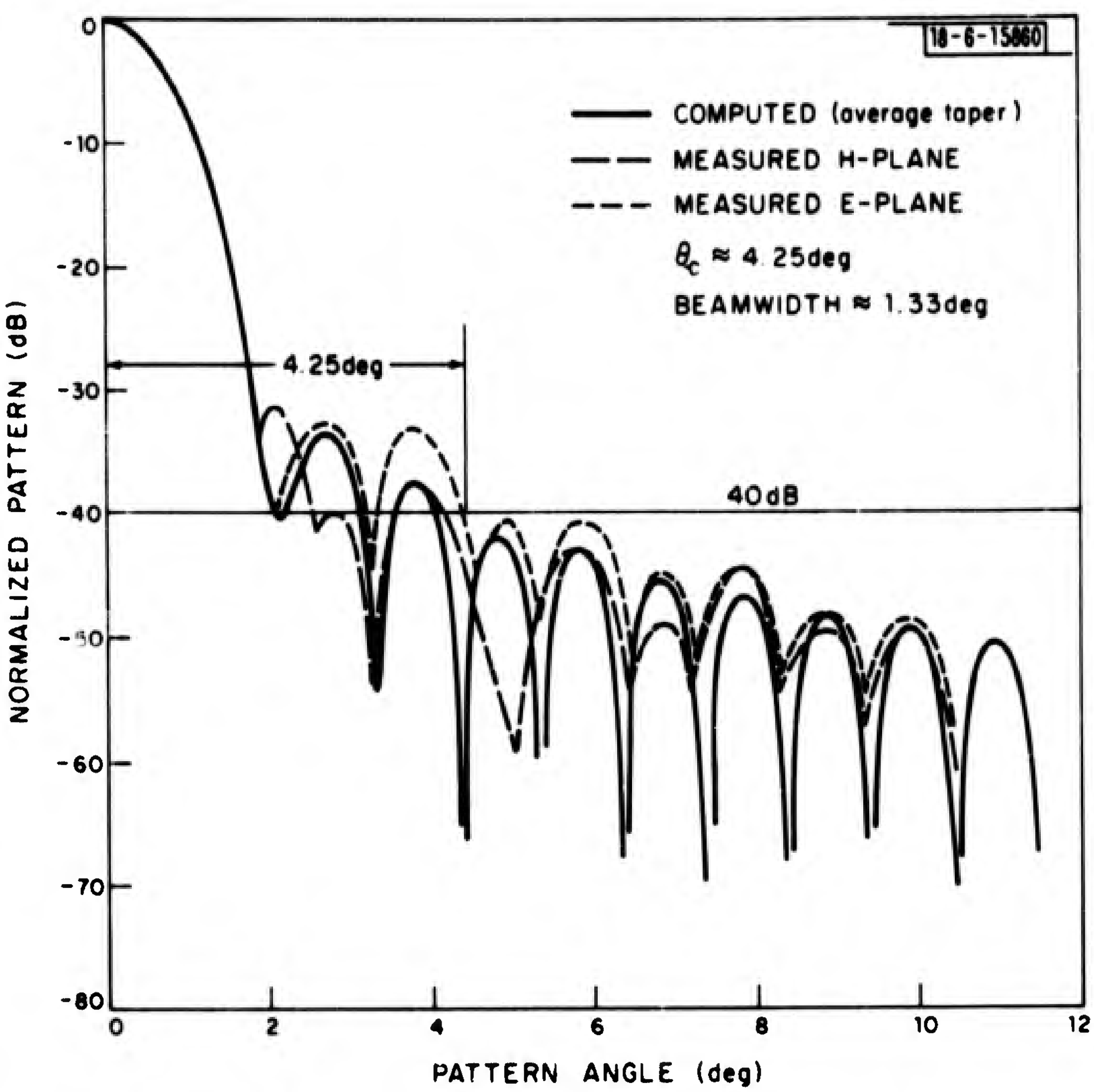

Fig. 11. Measured and computed radiation patterns for V-Band lens

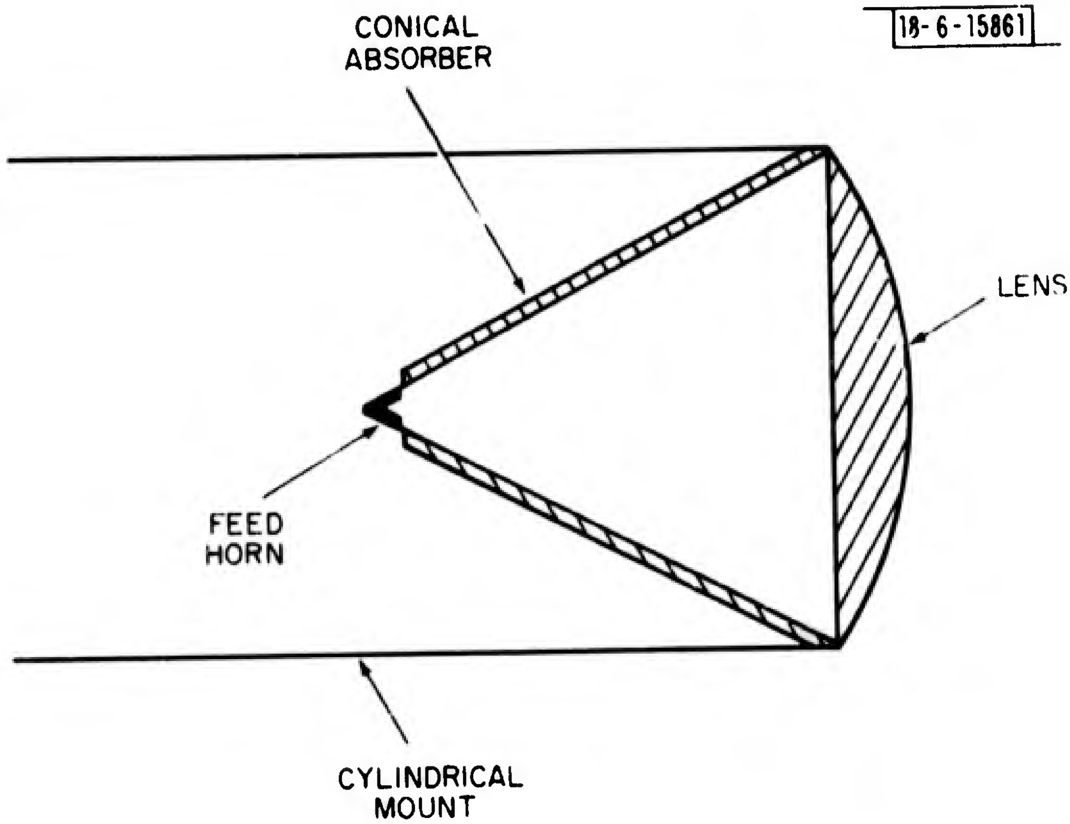

Fig. 12. Conical absorber mounted from feed to V-Band lens.

nificantly affect the pattern. The results are shown in Fig. 13. The complete sidelobe structure has decreased significantly, and the critical angle has decreased to approximately 3.4°, a significant improvement. The E-plane pattern is defocused somewhat, perhaps due to phase shifts introduced by the conical absorber. The presence of the absorber results in a gain decrease of roughly .5 to .75 dB.

D. V-Band Parabolic Dish--Experimental Results

The scaled V-band dish was initially used with a waveguide feed crossing over half the aperture diameter in the H-plane. The feed approximates an 18-dB taper at the edge of the dish. The dish was a commercial TRG 12-inch dish with the feed redesigned in order to fit inside the radome enclosure mentioned previously. The measured patterns are shown in Fig. 14. The principal plane patterns are significantly greater than 40 dB in the sidelobe region, indicating the need for an axial feed in the final design. The effect of feed scattering results in a critical angle of approximately 16° dominated by the E-plane pattern, where feed scattering is the most significant.

In view of the above results, an axially symmetric corrugated cup, rear feed design used previously at K_a-band[3] was scaled to V-band. The same 12-inch TRG dish was modified for use with this feed, and the dish and feed are illustrated in Fig. 15. The corresponding measured E- and H-plane patterns are illustrated in Fig. 16. The critical angle is now reduced to 8°. This critical angle is still significantly greater than that obtained with the lens, but is adequate for evaluating the effects of the radome enclosure on the outer sidelobe structure.

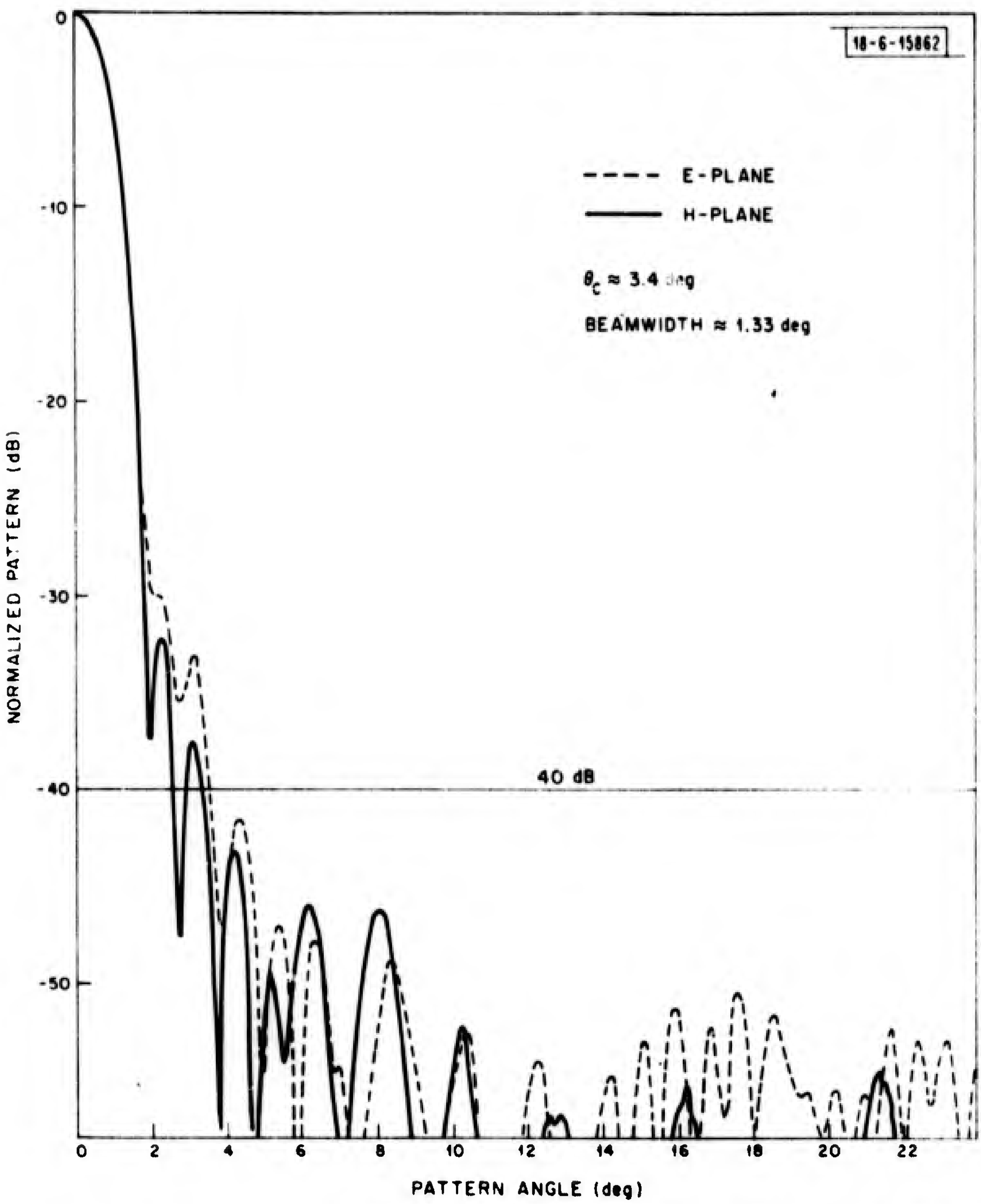

Fig. 13. Measured radiation patterns for V-Band lens -- with conical absorber.

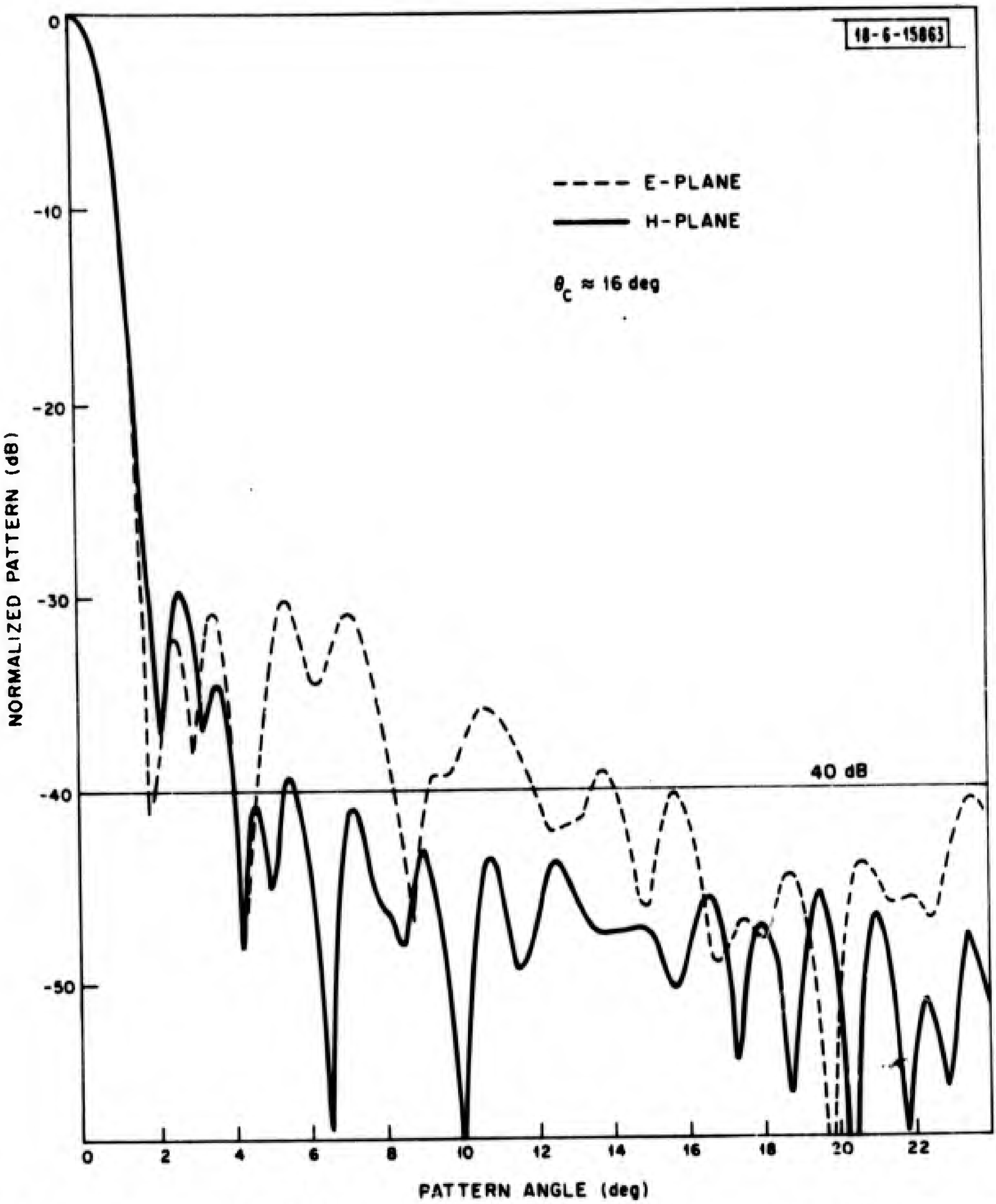

Fig. 14. Measured radiation patterns for V-Band dish -- over the rim wave-guide feed.

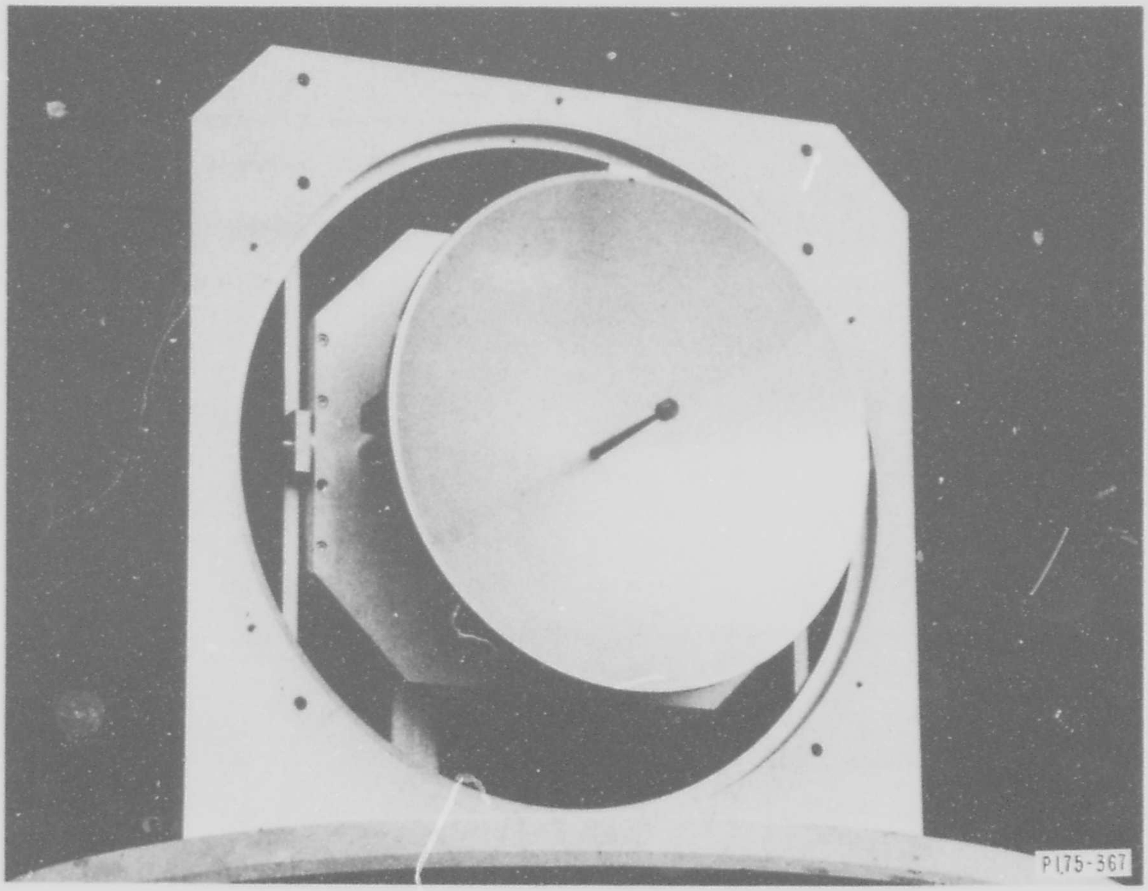

. Fig. 15. V-Band dish with axially symmetric feed.

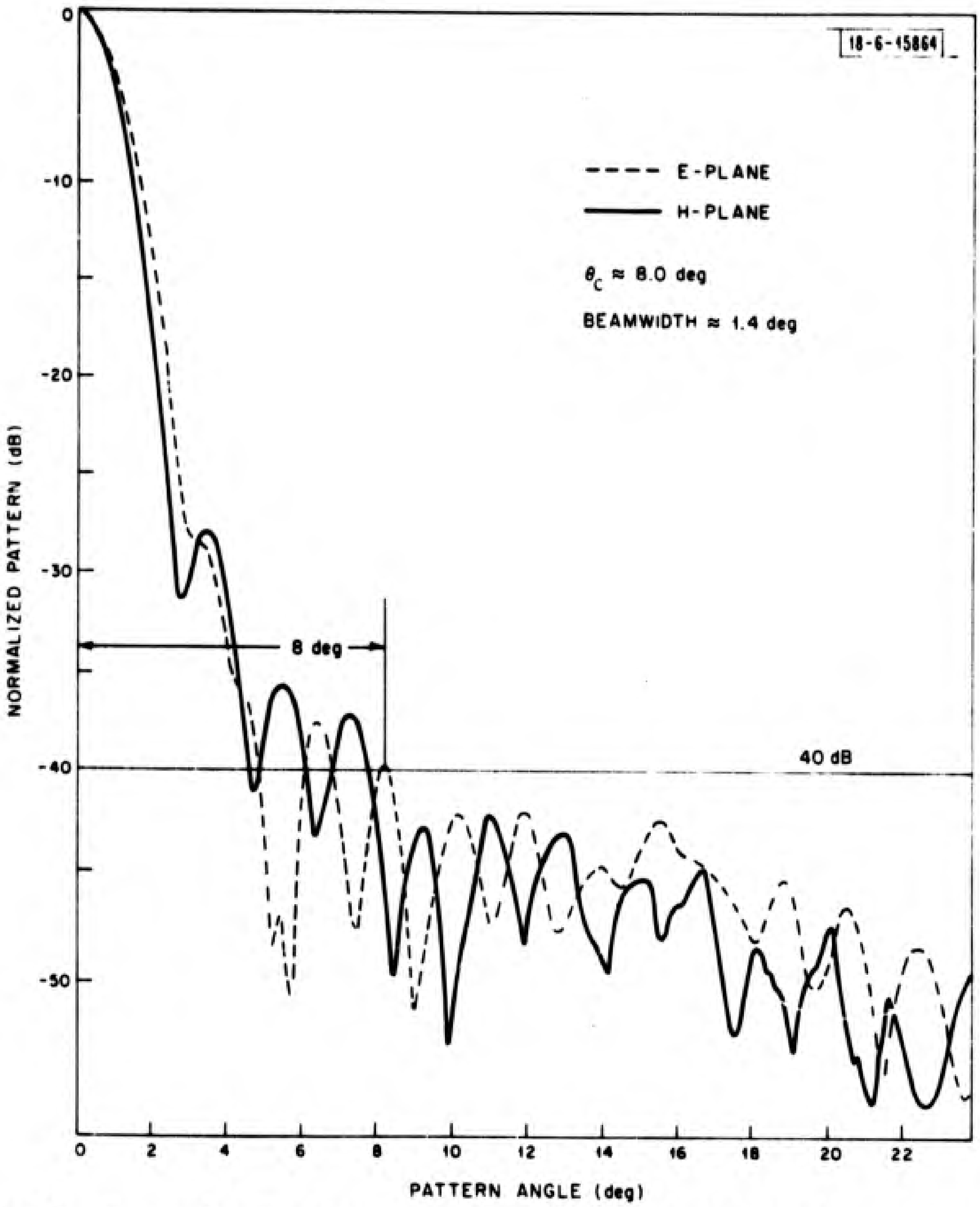

Fig. 16. Measured radiation patterns for V-Band dish with axially symmetric feed.

E. Effects of Aperture Blockage

The previous results have indicated that either an 18-inch lens or dish could be made to satisfy the low sidelobe requirements of the submarine antenna terminal, although, as expected, the lens yields a somewhat better sidelobe structure since the feed pattern is considerably easier to control. Thus it remains to examine the various other tradeoffs which might exist between the lens and the dish. One such tradeoff is the effect of antenna size on sidelobe level, where for the dish antenna the effect of feed blockage becomes important.

As the diameter of the aperture decreases, the feed used with the dish antenna occupies an ever increasing fraction of the total aperture area and hence feed scattering then becomes significant. In order to assess the magnitude of this effect, we have computed the critical angle outside which the field drops below 40 dB for a circular aperture with and without feed blockage, as a function of aperture diameter. The diameter of the feed blockage is fixed at .7 inch (the K_a-band diameter of the cup feed used above) and a $\cos^{4.5}$ taper was used for each case giving 40 dB first sidelobe without feed blockage. The results are shown in Fig. 17. Significant feed scattering is evident for aperture diameters less than 14 inches. Hence the use of an axially fed dish would require at least a 14-inch aperture.

III. Effects of a Spherical Radome on the Radiation Pattern of the Isolated Antenna

In order to estimate the effects of the radome on the sidelobe characteristics of the lens antenna, a computer program was written to calculate the

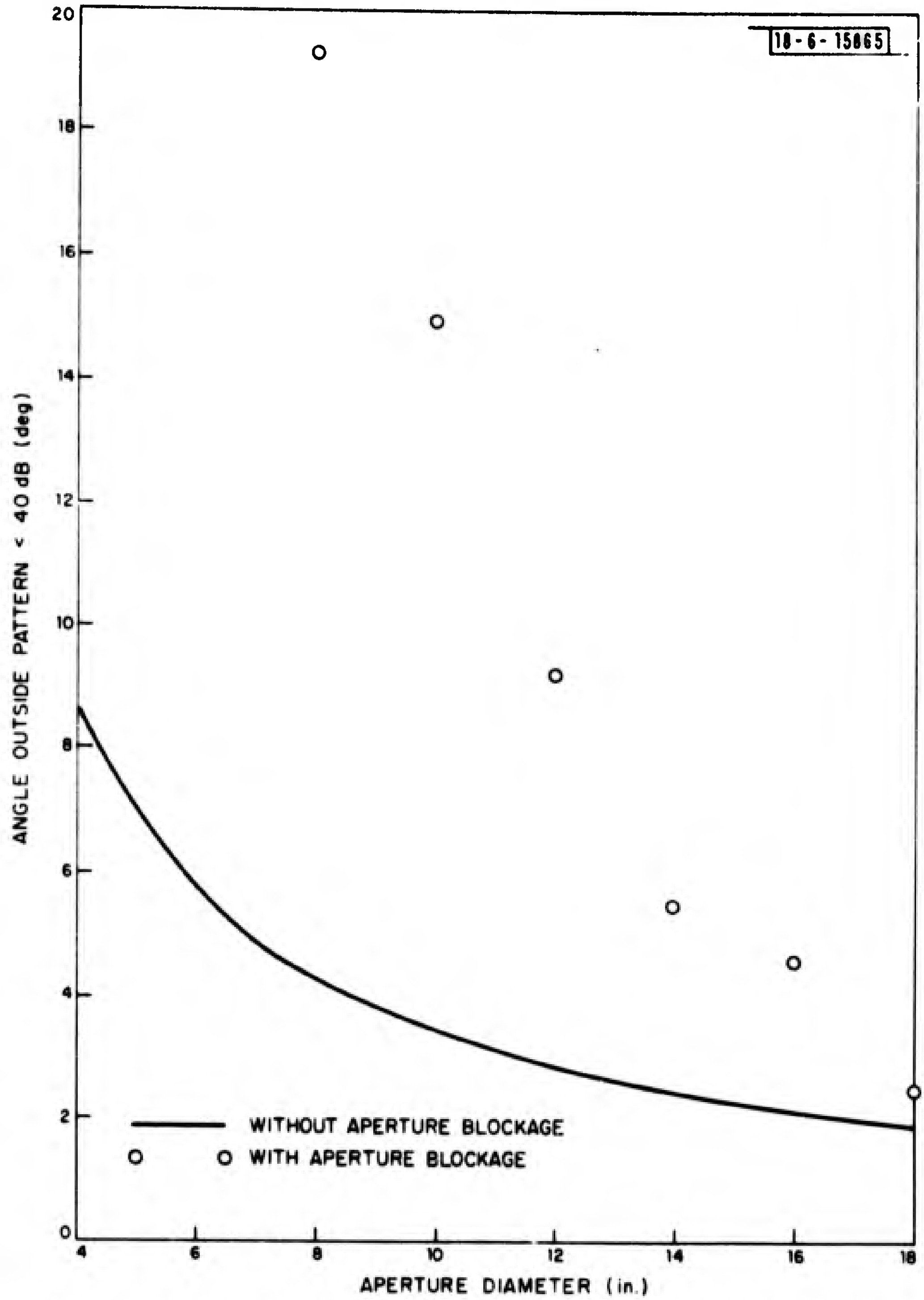

Fig. 17. Effects of feed blockage on 40 dB critical angle.

antenna radiation pattern with and without radome present. The details are presented in Appendix II. Referring to the geometry of Fig. 18, the incident wavefront is transformed through the radome via ray tracing to an effective aperture outside the radome, from which the far-field pattern is then calculated. The radome was made of Pyrex ($\varepsilon_r \approx 4.5$, $\tan\delta \approx 0.1$ at 37 GHz) and the thickness was chosen so as to minimize the net loss in gain due to absorbed and reflected power. The details of the calculation are presented in Appendix III. We have used a thickness of .688 inch at 37 GHz which maximizes the power transmitted through the radome and yet is thick enough to be representative of what one might expect for the final design of a structurally sound radome for submarine use.

The radome introduces significant phase distortion over the effective aperture outside the radome, and also introduces amplitude variations and a cross-polarized component over the aperture. Figure 19 compares the computed principal plane patterns with and without radome for the conical feed taper used with the 10-inch V-band lens considered earlier. The patterns with radome have differing E- and H-plane patterns, and the critical angle increases slightly, from 4.1° to 4.8°. Figure 20 illustrates the cross-polarized component of the radiation pattern, with radome, along the diagonal (45°) plane where the cross-polarization is maximum. The radome does not introduce a cross-polarized component in the principal planes. Insertion of the radome introduces 1.92 dB loss in gain (calculated). Thus for the lens antenna, where multiple radome-lens reflections can be expected to have a negligible amplitude, a homogeneous spherical radome should not introduce significant

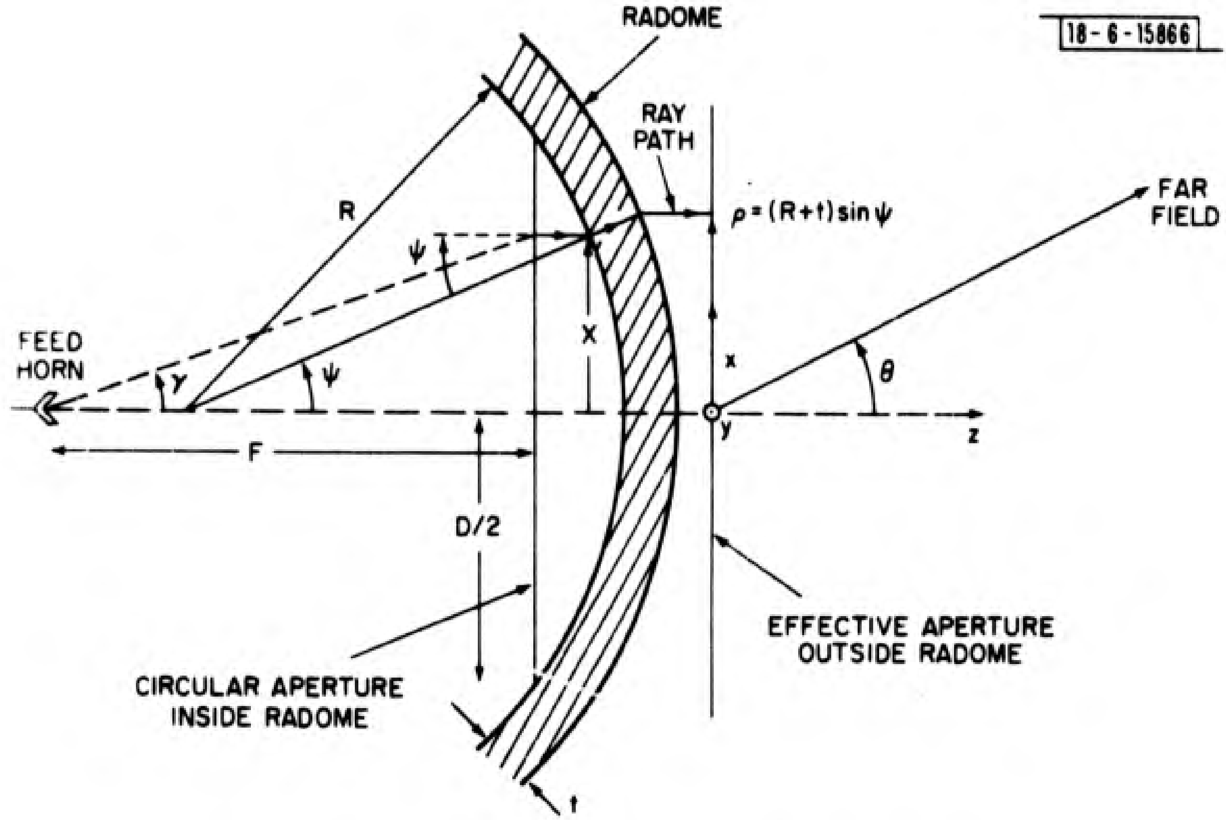

Fig. 18. Geometry for calculating effects of spherical radome on the radiation pattern.

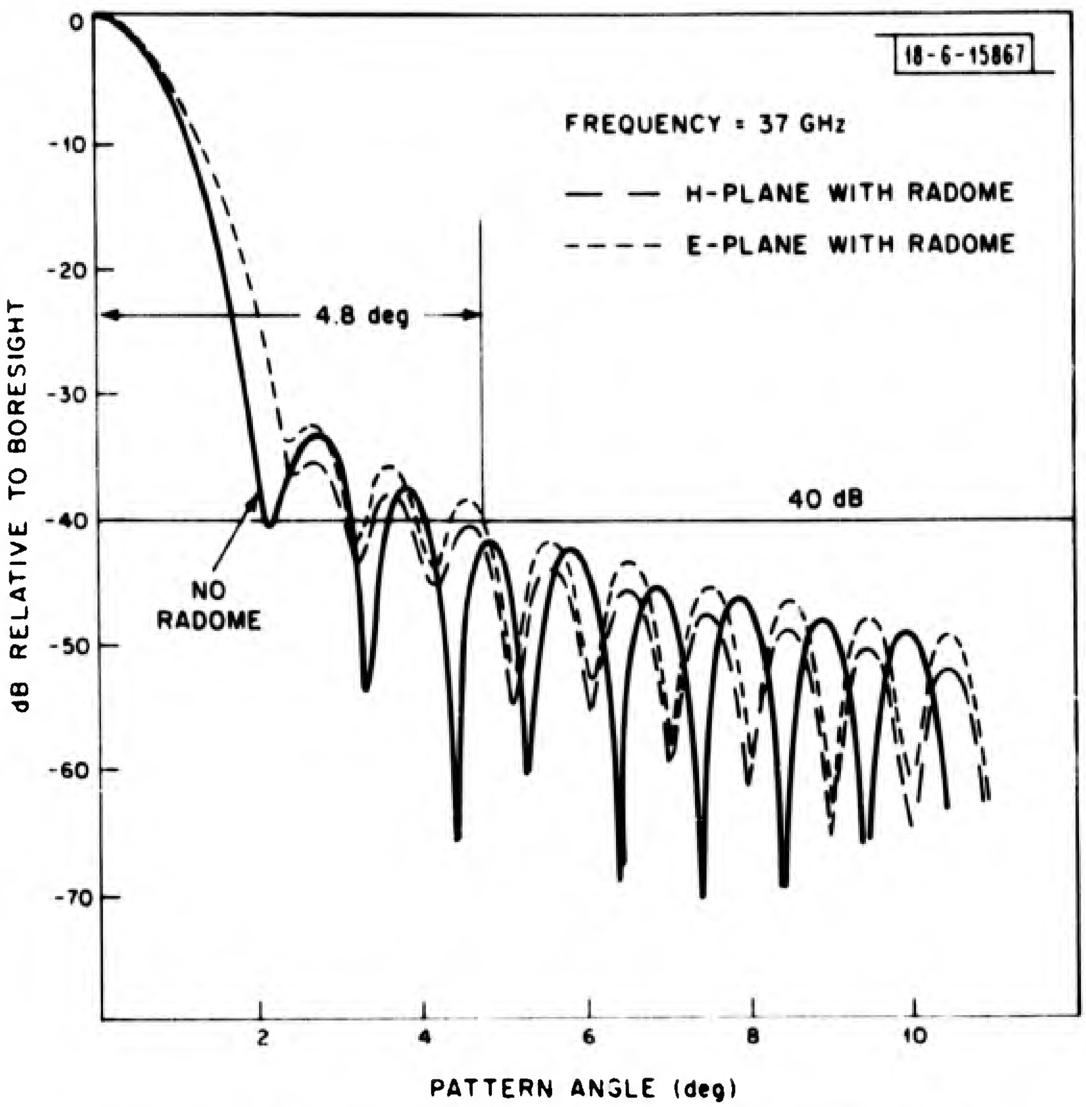

Fig. 19. Calculated radiation patterns for pyrex radome.

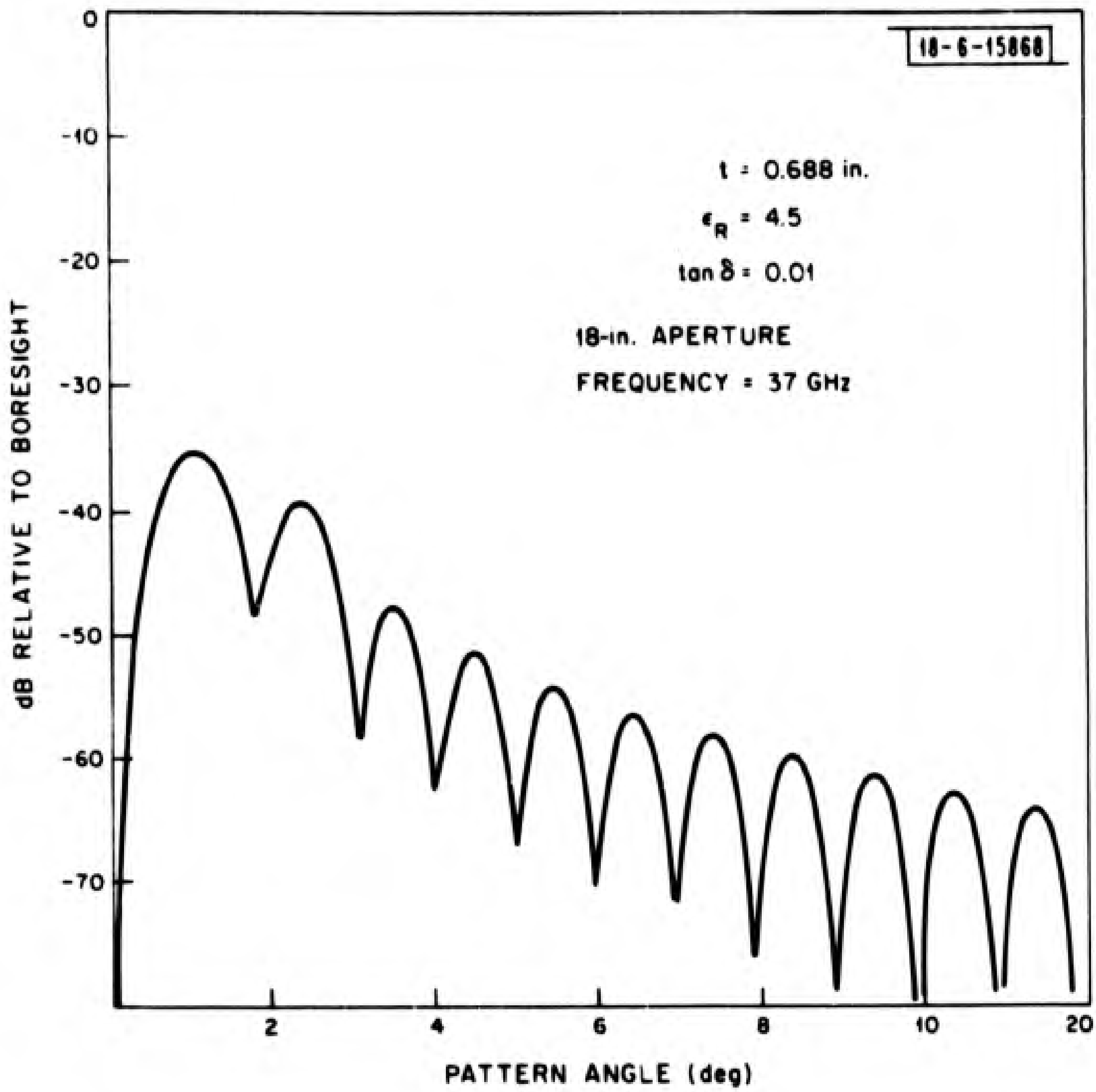

Fig. 20. Cross-polarization introduced by pyrex radome in diagonal (ϕ = 45°) plane.

pattern distortion, and should not increase the critical angle significantly. These conclusions will be verified in the following discussion of the experimental results.

A. Measured Patterns for the V-Band Lens Inside a Pyrex Radome

In order to verify these conclusions experimentally, a hemispherical Pyrex radome was constructed to fit over both the lens and dish antennas. The thickness was scaled to .417 inch at 61 GHz from .688 inch at 37 GHz. The combination lens-radome mounting is shown in Fig. 21. The corrugated V-band horn discussed previously was used as a feed, and the measured radiation patterns with and without radome are illustrated in Figs. 22 and 23. As expected the phase distortion introduced by the radome eliminates the near-in sidelobes, but the critical angle has increased from 4.25° to approximately 6°, slightly greater than expected. This phase distortion can be partially compensated for by refocusing the feed in which case the critical angle is found to decrease to approximately 5.4°. In Figs. 24 and 25 the radiation patterns with and without radome are illustrated for the case when the conical absorber is present from the feed to the outer diameter of the lens. The pattern distortion introduced by the radome is now significantly less, and the critical angle has only increased .4°, from 3.4° to 3.8°. Thus it appears feasible to satisfy the low sidelobe requirement both with and without radome if one uses a lens antenna enclosed by a homogeneous radome. The presence of the radome results in a gain loss of 3 dB, somewhat greater than calculated.

B. Measured Patterns for V-Band Dish with Spherical Radome

The results for the dish-radome interaction are not as encouraging. Figure 26 illustrates the measured patterns for the V-band dish with axially

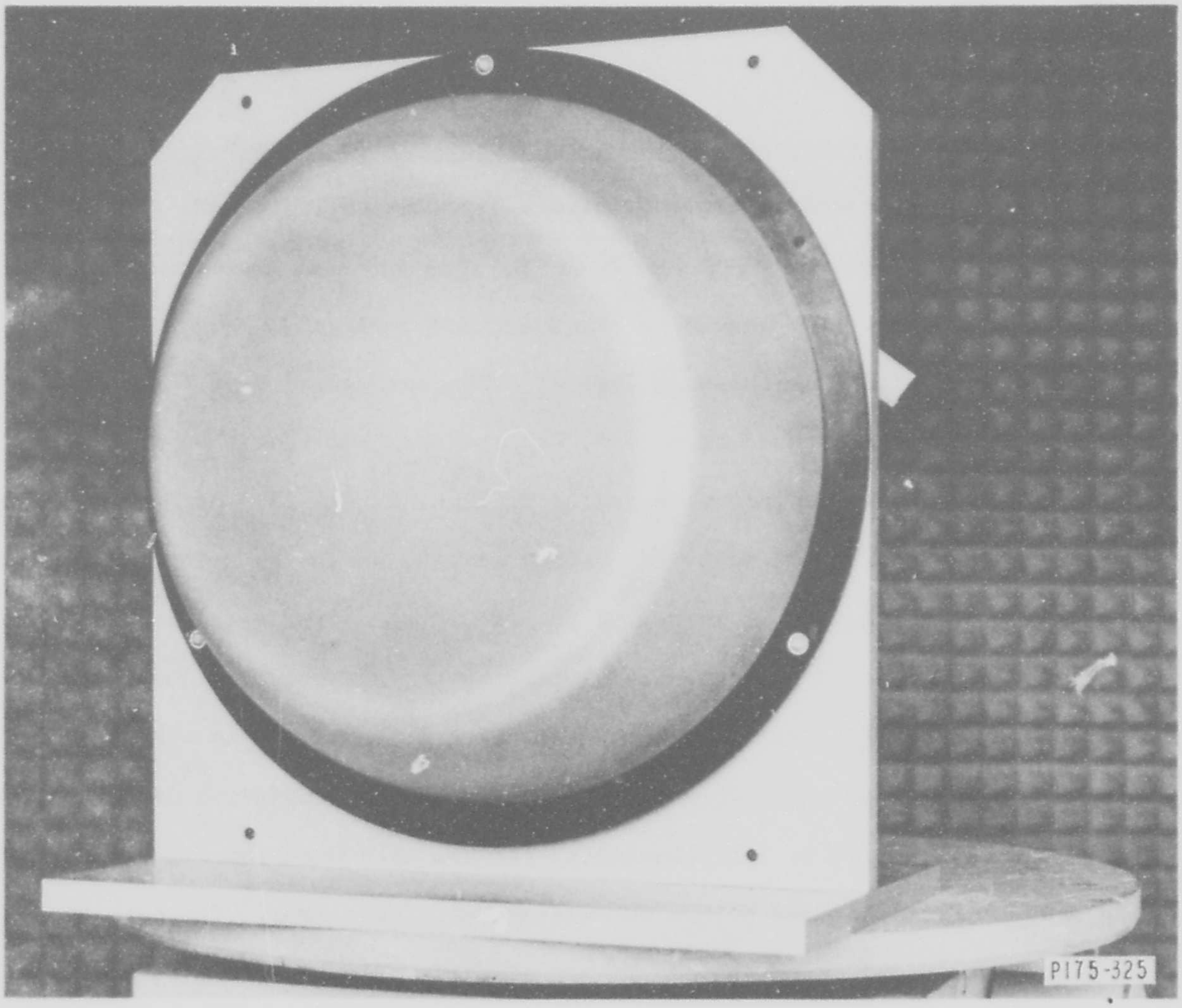

Fig. 21. V-Band lens inside spherical radome.

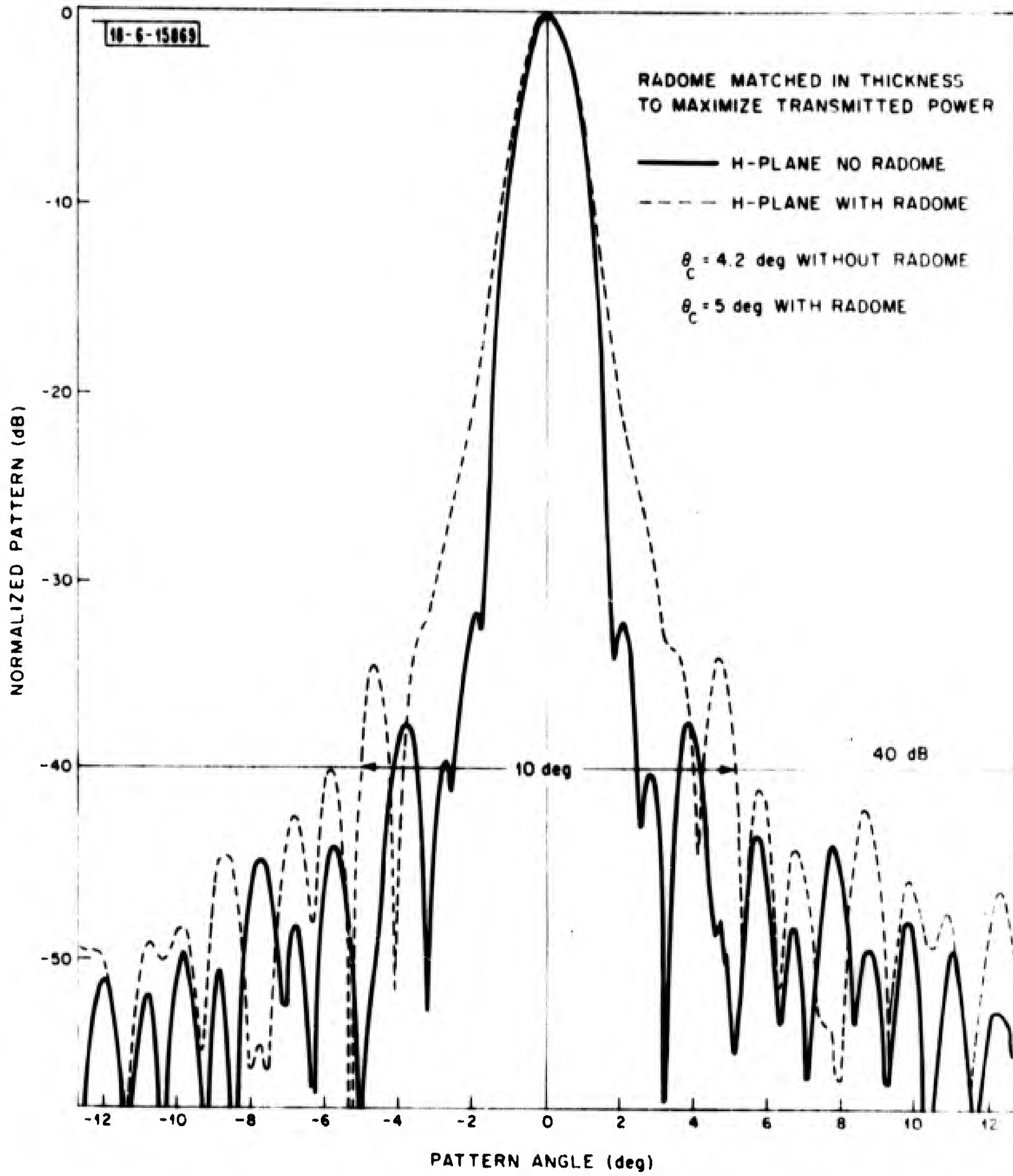

Fig. 22. Measured effects of radome on H-plane radiation pattern of V-Band lens.

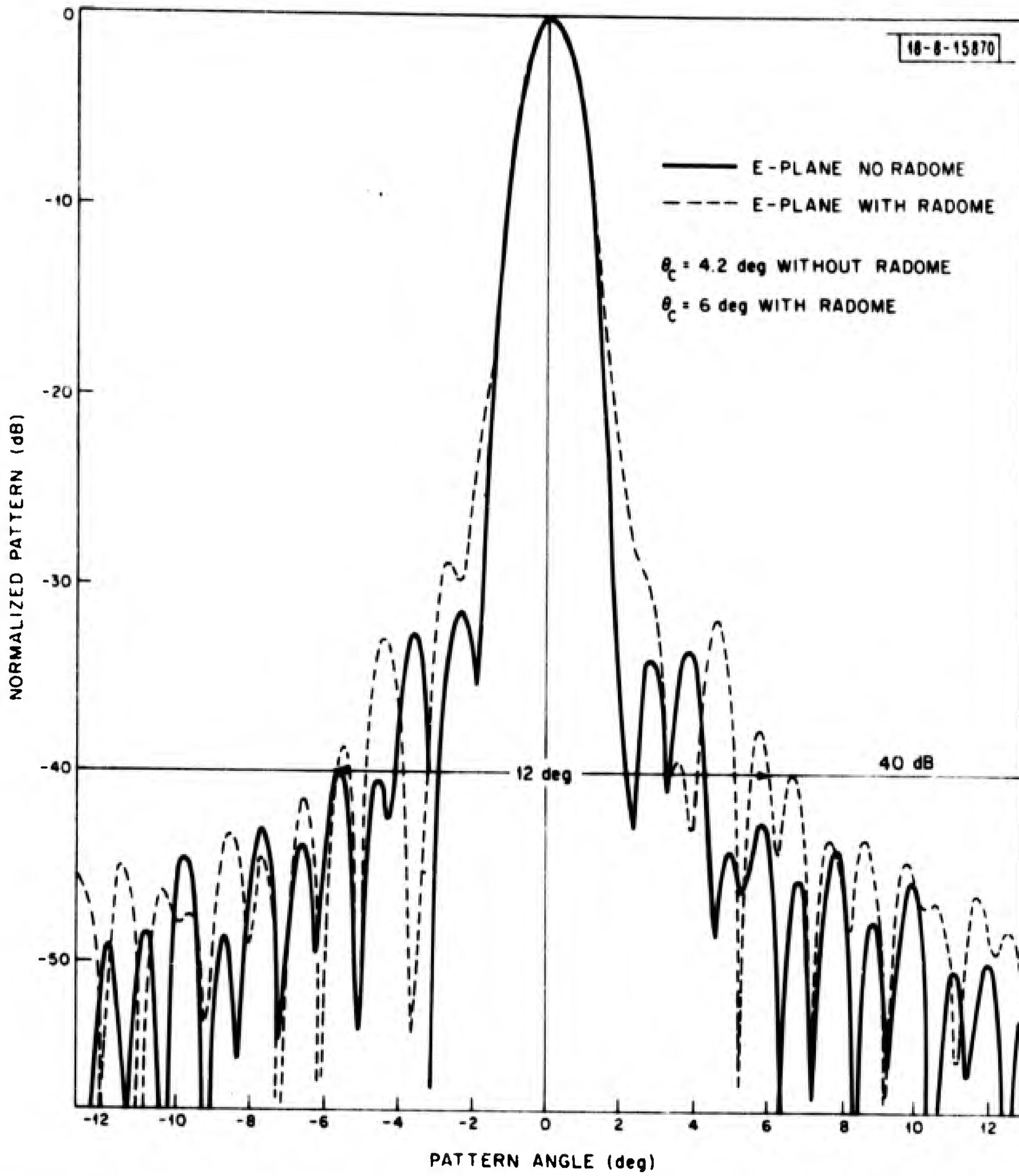

Fig. 23. Measured effects of radome on E-plane radiation patterns of V-Band lens.

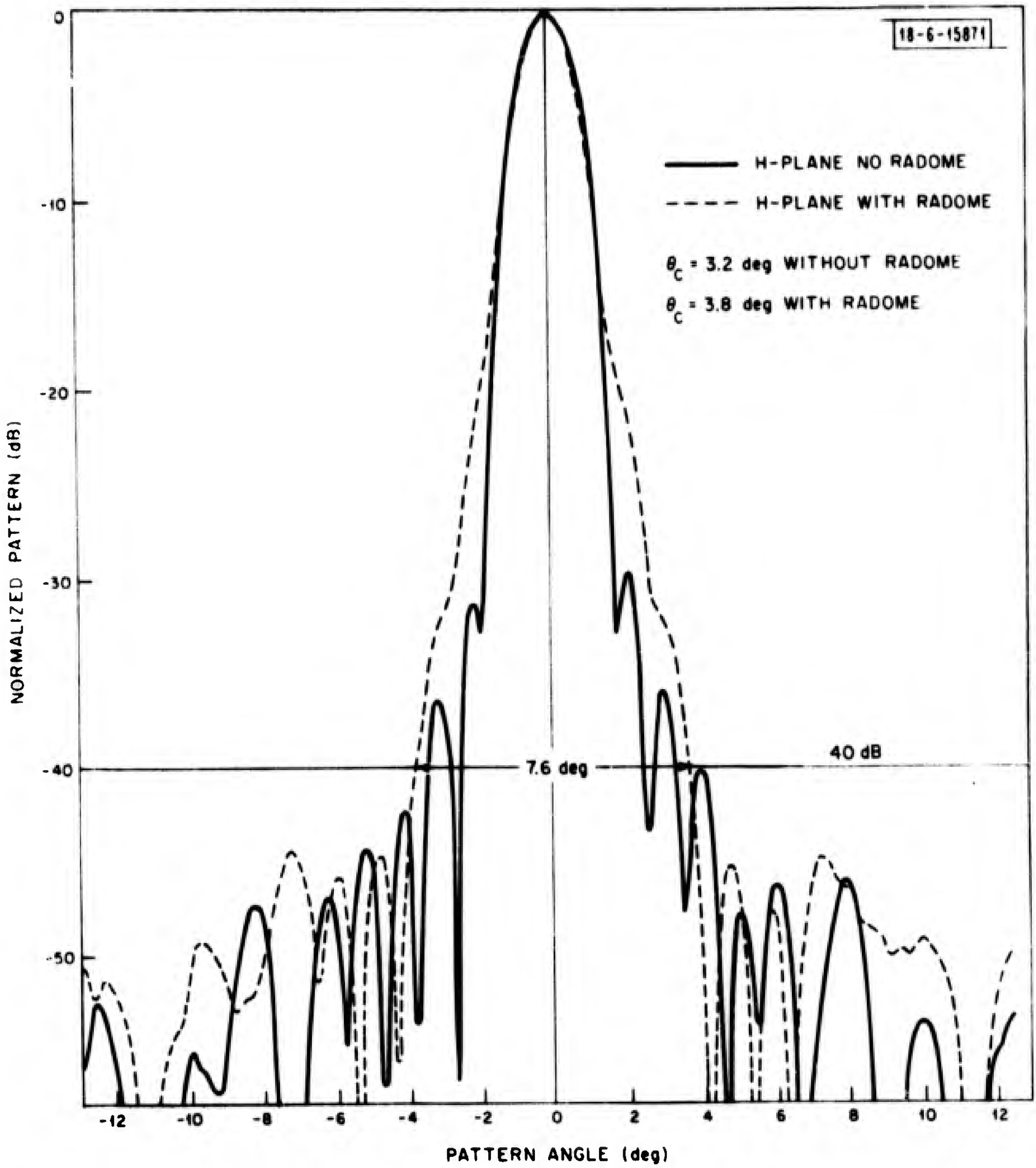

Fig. 24. Measured effects of radome on H-plane radiation pattern of V-Band lens.

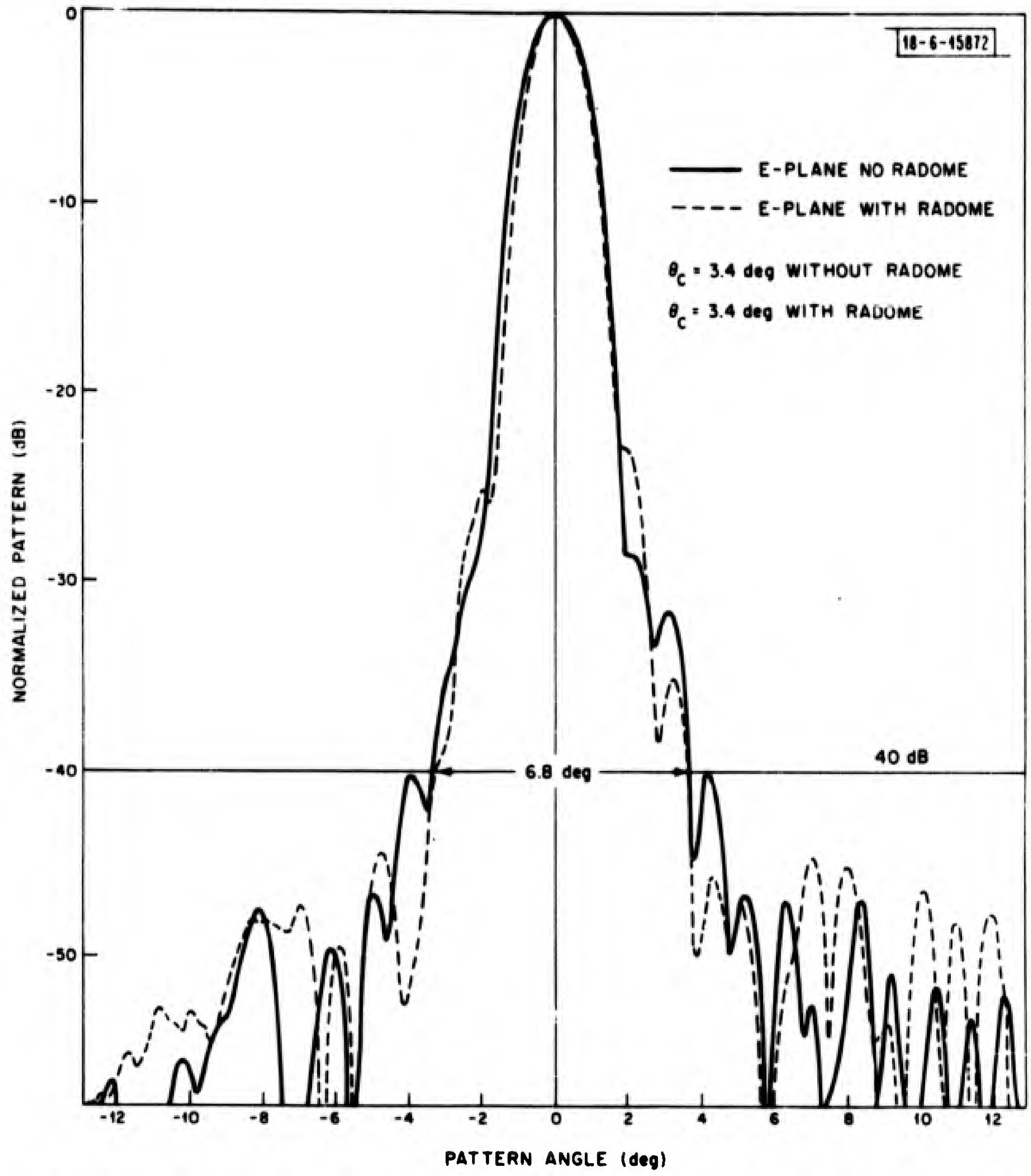

Fig. 25. Measured effects of radome on E-plane radiation pattern of V-Band lens -- with conical absorber present.

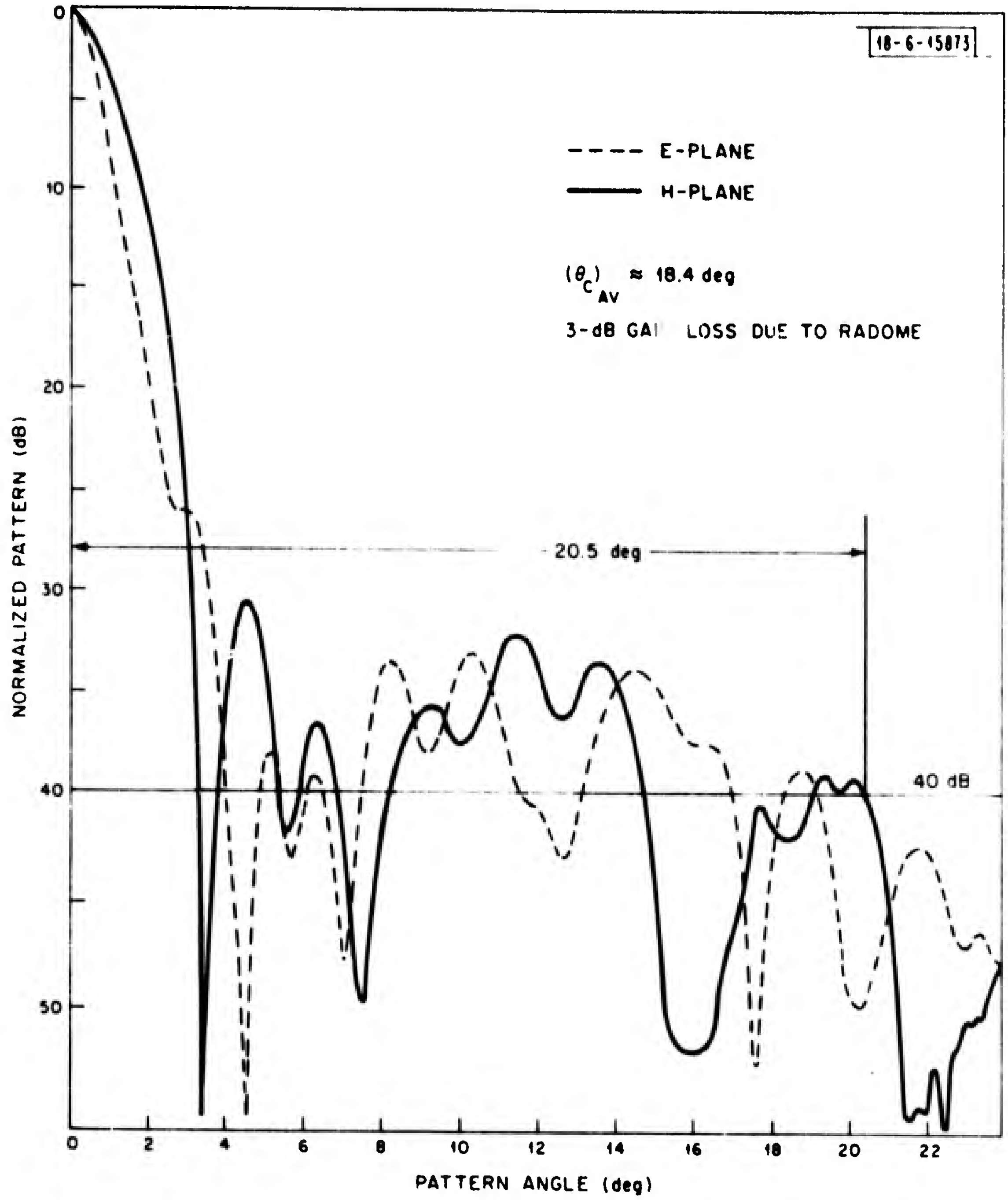

Fig. 26. Measured radiation patterns for V-Band dish with axial feed -- with radome.

symmetric feed, enclosed by the spherical radome. We observe that the multiple reflections between dish and radome account for significant scattering into the sidelobe region. The critical angle has increased from 8° to approximately 20°. This, of course, would be expected, as with the dish, all the energy radiated from the feed (other than spillover) must exit to the far field; with the lens, some of the reflected energy passes back through the lens and is absorbed in the enclosing structure. This suggests that it might be possible to lower the sidelobe level with radome by employing individual matching layers on each side of the radome. This would further reduce the energy reflected from the radome, which scatters into the sidelobe region. A combination of polyethylene ($\varepsilon_r \approx 2.24$) and paraffin wax ($\varepsilon_r \approx 2.22$) were used as matching layers. The results are shown in Figs. 27 and 28 for the cases with and without radome for the principal planes. The critical angle has decreased significantly, to approximately 12°, although the power level remains near the 40-dB level out to approximately 18°.

C. Measured Cross-Polarization Introduced by the Radome

As mentioned above, the radome does introduce a significant cross-polarized component along the diagonal planes, but no cross-polarized component in the principal planes. This in fact was observed experimentally. A contour plot verified that the radome only increased the peak cross-polarization level about 1-2 dB. Furthermore, the position of the maximum lies close in toward the main beam, and well within the critical angle of the main beam. Thus the cross-polarization introduced by the radome should not be a major factor in the sidelobe level outside the critical angle.

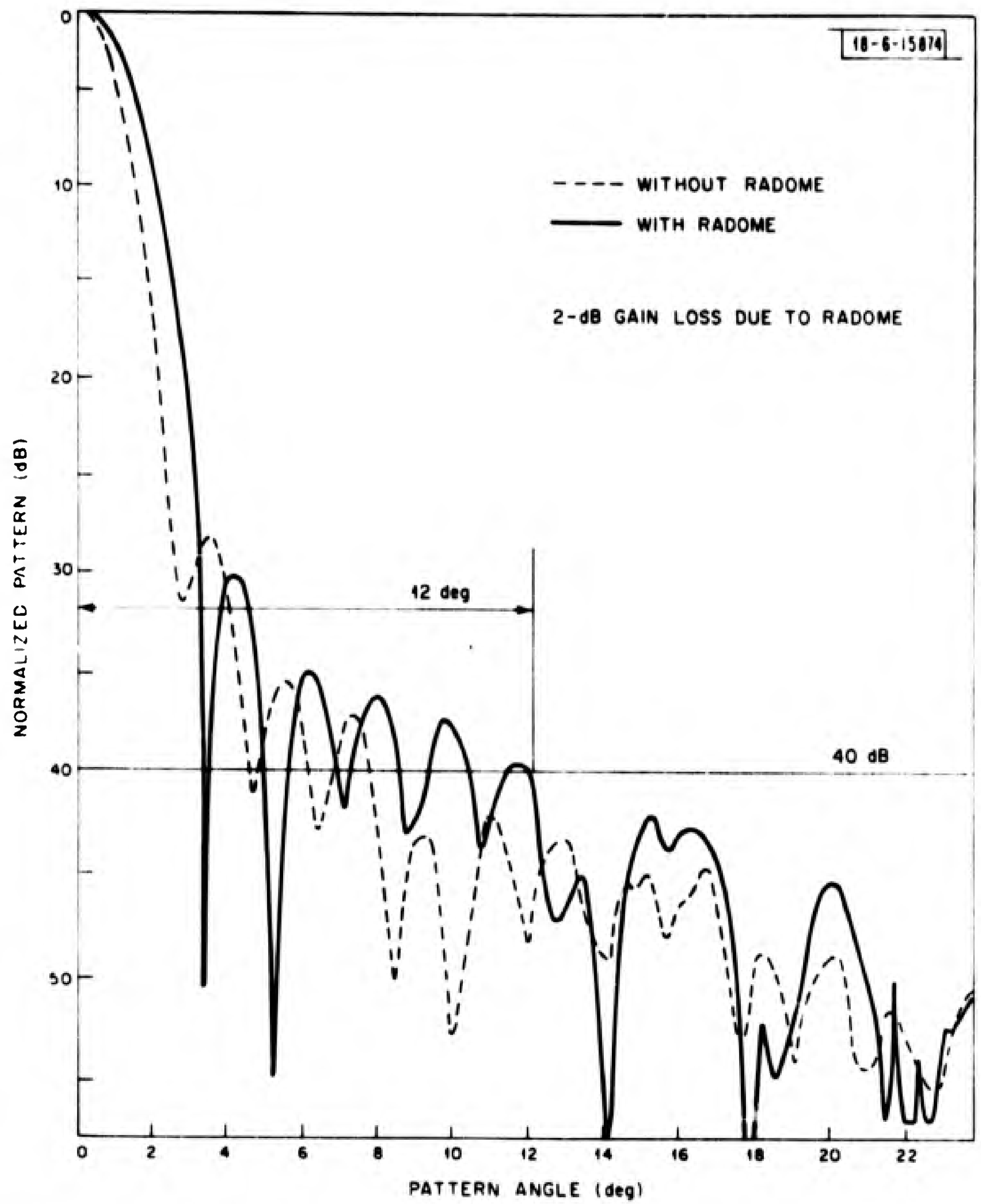

Fig. 27. Measured H-plane radiation patterns for V-Band dish with axial feed -- with radome with matching layers.

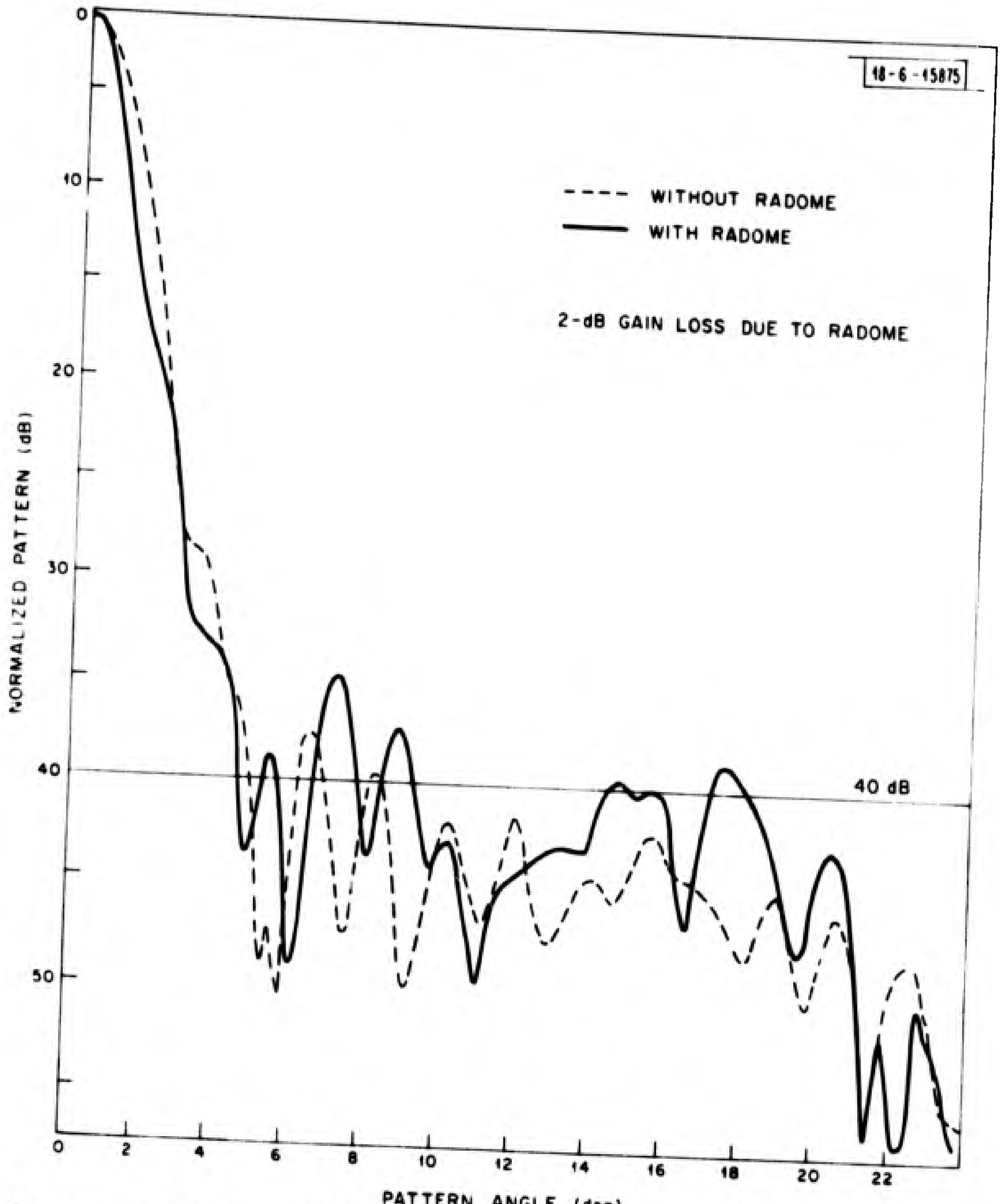

Fig. 28. Measured E-plane radiation patterns for V-Band dish with axial feed -- with radome with matching layers.

IV. Conclusions

We have examined the problem of the feasibility of designing a low-sidelobe antenna-radome combination to be used in a submarine environment. Physical considerations require that the antenna be of minimum size, yet have the lowest possible sidelobe structure. We have shown that the choice of an 18-inch aperture yields a good tradeoff of aperture size vs. sidelobe level, and that at f = 37 GHz, the best theoretically achievable critical angle outside which the pattern is below 40 dB is 1.8°, with a beamwidth of 1.3°. In order to examine how closely one can expect to approach the ideal result, we have tested four candidate antennas having a low sidelobe structure, two lenses and two paraboloidal reflectors (dishes). With moderate care, we have been able to achieve a critical angle of 3.4° with a lens antenna and 8.3° with a dish, incorporating an axially symmetric feed. These certainly do not correspond to the theoretical lower limit, but are felt to be adequate within scope of the present study. The 40-dB critical angle has been used only as a convenient measure to compare the outer sidelobe level. In Table I, we present a more detailed comparison of the lens vs. the dish in which we consider not only the 40-dB critical angle, but also the 50-dB critical angle, beamwidth and the corresponding quantities for the cross-polarized component. For comparison, we also include in the table the corresponding data for the K_a-band, 18-inch dish[(3)] from which the V-band dish was scaled. It is clear that the lens offers a much lower outer sidelobe pattern. Furthermore, it has been shown[(3)] that the 8° critical angle for the axially symmetric dish is due primarily to aperture blockage and surface roughness. Thus it appears

Table 1

COMPARISON OF DISH TO LENS

	LENS	DISH-AXIAL FEED
Beamwidth	1.35°	1.4° (1.5°)$^{+}$
40 dB Critical Angle	3.4°	8.3° (8°)$^{+}$
50 dB Critical Angle	8.5°	24° (17°)$^{+*}$
40 dB Critical Angle with Radome	3.8°	15° (Average)
Cross-Polarization Level below Principal Component	28 dB	10 dB^{+}
$(\theta_c)_{40dB}$ Cross Polarization	2.7°	5°$^{+}$
$(\theta_c)_{50\ dB}$ Cross Polarization	4.5°	9°$^{+*}$

$^{+}$ = Measured on 18-inch K_a-band antenna (37 GHz) - Principal E and H planes only.

* = Neglects slight peak at 50 dB off edge at 90°.

that it would be difficult to improve significantly on the 8° value for the dish. Since there is no aperture blockage with the lens, one has much better control over the aperture distribution, and hence a greater freedom to lower the sidelobe level. Thus the lens offers definite advantages over the dish in minimizing the sidelobe level. The one advantage of the dish antenna is that it takes up less volume than the lens, which might make it easier to package equipment inside the radome.

The effect on the radiation pattern of a spherical radome enclosure over the antenna was also studied. A homogeneous, spherical, Pyrex radome was designed for minimum reflection and absorption, and the effects on both the lens type and dish-type antennas were determined. For the lens, the radome did not significantly affect the sidelobe structure outside the critical angle of 3.8°, although the pattern is defocused somewhat in the main beam due to the phase errors introduced over the aperture due to the radome. Feed defocusing can be used to partially cancel out these phase errors, hence increasing gain and decreasing the critical angle.

When the radome enclosure is used with the dish-type antenna, the effect of dish-radome reflections lead to a significant increase in the sidelobe level. We were able to partially compensate for this increase by employing matching layers on each surface of the radome, although the outer sidelobe structure is still somewhat higher than the lens. The use of the dish necessitates the use of an axial type feed to minimize the effects of feed scattering and the effects of radome-feed interactions.

Acknowledgements

The authors are grateful for the valuable assistance of many of their associates. Particular thanks are due to Mr. Bernie La Page, who contributed to the initial phases of the antenna-radome study program; to Mr. Lee Niro, for his excellent programming of the numerical results; to Mr. Tim Stephens, for his excellent support in the mechanical design of the various components used in the experiments; and to Mr. Tom Guttadauro and Mr. Don Brown, who ably obtained the experimental results.

APPENDIX I

Lens Design

The design of a lens antenna is more complicated than that of a parabolic reflector, because the lens design has more variables. With both antennas, the diameter is usually fixed by system considerations, that is by the desired gain or beamwidth at the operating frequency. The only remaining parameter to be chosen for the reflector is the focal length. The lens has two refracting surfaces; one surface can be chosen almost arbitrarily, and the other then determined to give a desired focal length. In addition, another parameter is the dielectric constant the choice of which affects the thickness as well as the lens shape. Lens design is usually carried out using geometrical optics and neglecting interface reflections. In order to successfully neglect these reflections, a low dielectric constant is desired so that the complications of surface impedance matching layers can be avoided. The dielectric constant cannot be chosen too low, however, because if it is, a very long focal length or very thick lens will be required. In addition, the dielectric material must have a very low loss tangent at the frequency of interest to avoid excessive loss of energy, and also to avoid modification of the feed-horn illumination taper.

Materials commonly used for microwave lenses because of their low loss and reasonable dielectric constants are polytetrafluoroethylene (Teflon) and polystyrene. In our lens design we have used the latter in a stable, cross-linked, easily machined form sold under the trade name Rexolite 1422.

The index of refraction (ϵ'/ϵ_o) at 37 GHz is approximately 1.59 and loss tangent is less than .001.

Two lens shapes are easy to analyze.[4] The first is the plano-convex, with the convex side facing the feed, and the exit plane of the lens coinciding with the exit phase front. The convex side in this case is described by a hyperbolic curve. This lens tends to bunch the energy from the feed toward the center of the lens, increasing the amplitude taper. It has the disadvantage that the angles of incidence of the rays on the convex side are relatively large, leading to large reflections for one polarization for reasonable values of focal length. The second type of lens has a spherical inner surface, coinciding with the input spherical phase front from the feed horn. The outer surface is described by an ellipsoid of revolution. The main disadvantage of this lens is that it tends to bunch the energy at the edges of the lens and decreases the amplitude taper, tending to raise sidelobes. Both of these lenses have the disadvantage that one surface coincides with a phase front of the electromagnetic wa e and so any surface reflections tend to be focused back to the feed horn, possibly causing too high an input VSWR.

We have chosen a plano-convex lens, with the plane side toward the feed. This is a configuration somewhat more difficult to characterize analytically, but has desirable electrical properties. Refraction takes place at both surfaces, so angles of incidence of rays at these surfaces are relatively small, leading to relatively low reflection for any incident polarization. Neither surface is an equiphase surface, so reflection back into the feed tends to be small. This lens has little effect on the amplitude taper. The plane surface is relatively easy to machine. The curve describing the outer surface cannot be expressed in simple analytical form, but must be computed numerically.

The coordinates of points on the generating curve of the lens may be derived using the law that for a focused system, all electrical path lengths from the feed to a prescribed aperture plane are equal, and also using Snell's law at the plane surface, that is (see Fig. I-1)

$$P_{01} + n\,P_{12} + P_{23} = F + nt \tag{I-1}$$

$$n\sin\Psi = \sin\theta \tag{I-2}$$

where P_{01} is the distance from the focus to the plane surface of the lens

P_{12} is the path length of the ray inside the lens

P_{23} is the path length from the lens to the reference plane

θ is the angle of incidence

Ψ is the angle of refraction

n is the index of refraction, $n = \sqrt{\varepsilon'/\varepsilon_o}$

t is the lens thickness at center.

After some manipulation, parametric expressions for the x, y coordinates of the lens generating curve can be found:

$$x = \frac{F\cos\Psi(\cos\theta-1) + t\cos\theta\cos\Psi(n-1)}{\cos\theta(n-\cos\Psi)} \tag{I-3}$$

$$y = \frac{F\sin\theta(n^2-n\cos\Psi + \cos\theta - 1) + t\cos\theta\sin\theta(n-1)}{n\cos\theta(n-\cos\Psi)} \tag{I-4}$$

The thickness, t, required can be considered a function of the maximum diameter, $2y_{max}$, of the lens and the focal length F. For the edge ray, the path $P_{12} = 0$ and (I-1) can be written as

$$(F^2 + y^2_{max})^{1/2} + t = F + nt$$

which may be solved for t

$$t = \frac{(F^2 + y^2_{max})^{1/2} - F}{n-1} \tag{I-5}$$

If a given aperture diameter antenna is desired, $2y_{max}$ is chosen slightly larger so that a rim thickness is available at the edge of the lens for attachment purposes. In addition, y_{max} may be adjusted slightly so as to make $nt \cong m\lambda/2$, m an integer, which condition reduces the reflection for the paraxial rays. Equation (I-5) may be cast in the form

$$\frac{t}{D} = \frac{((F/D)^2 + 1/4)^{1/2} - F/D}{n-1} \tag{I-6}$$

where $D = 2y_{max}$ and plotted for a typical value of n, n = 1.59. (See Fig. I-2.) From this curve, it can be seen that F/D cannot be much less than unity to maintain a reasonably small value of t. F/D must also be kept near unity to keep the angles of incidence of the edge rays from getting too large, so that reflection does not become a severe problem. On the other hand, it is desirable to keep F as small as feasible to make the overall antenna design more compact.

It remains only to calculate the effect of the lens on the amplitude taper. Given an amplitude distribution $A(\theta)$ from the feed horn, we wish to find the aperture amplitude distribution $F(y)$. From Ref. 4

$$\frac{F(y)}{A(\theta)} = \left[\frac{\sin\theta d\theta}{ydy}\right]^{1/2}$$

$dy/d\theta$ may be obtained by differentiating I-4 with the result that

$$\frac{F(y)}{A(\theta)} = (nF + t)\left[\frac{\sin\theta\cos\theta(n-\cos\Psi)}{nyU}\right]^{1/2} \tag{I-7}$$

where $U = F\cos\theta(n^2-\cos\Psi + \cos\theta - 1) - F\sin\theta(\sin\theta-\cos\theta\tan\Psi)$

$$+ t(n-1)\cos2\theta + ny\sin\theta(n-\cos\Psi) - y\cos^2\theta\tan\Psi.$$

When evaluated numerically, this ratio varies little from unity for the lenses studied ($F/D \cong 1$). Figure 3 shows calculated values of this factor using the parameters for the final lens design. Observe that even at the outer edge of the lens, the feed pattern is only modified by .735 dB.

For the present application, an aperture diameter of 18 inches was required. To obtain a usable 18-inch aperture, D in (I-6) was chosen as 19 inches, and F as 15, ($F/D \cong .8$) leading to a center thickness of 4.66 inches. These values were chosen as an engineering compromise among the various factors mentioned above.

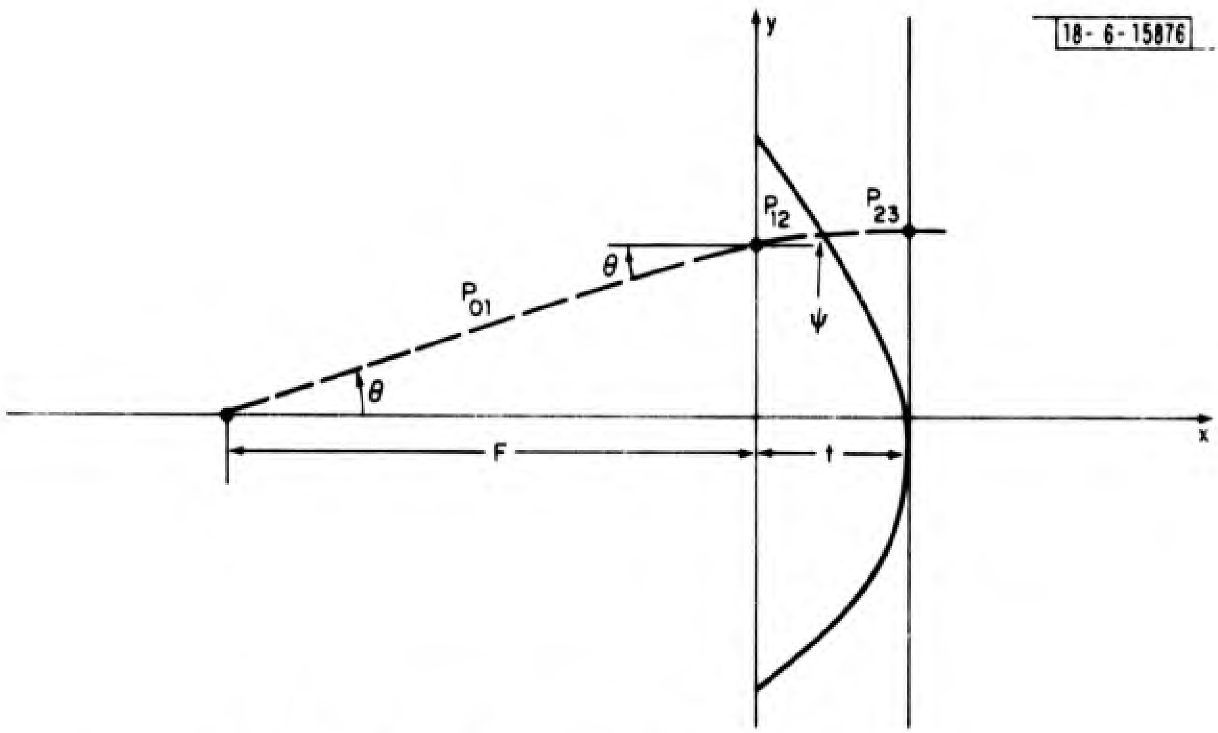

Fig. I-1. Geometry describing plano-convex lens.

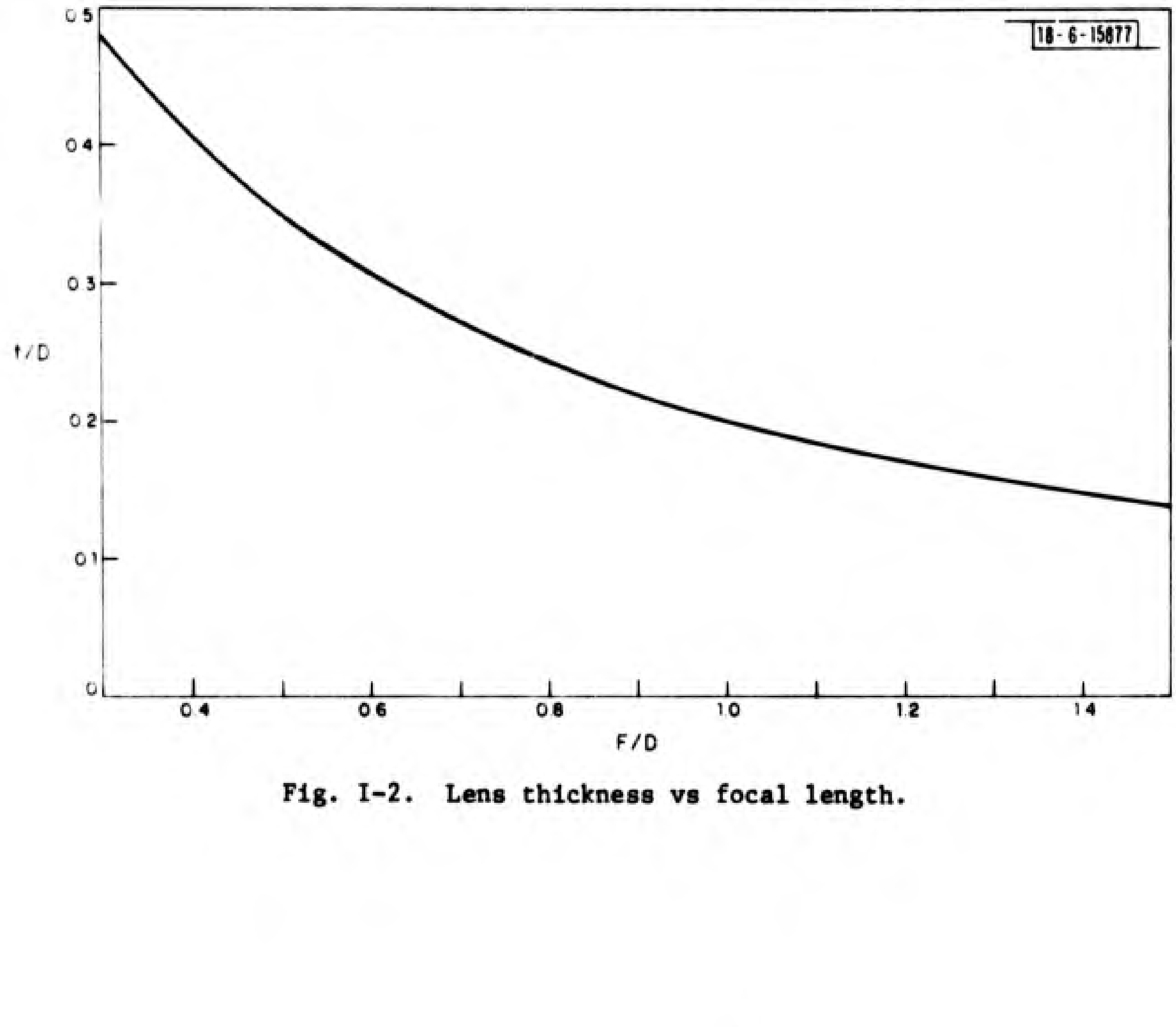

Fig. I-2. Lens thickness vs focal length.

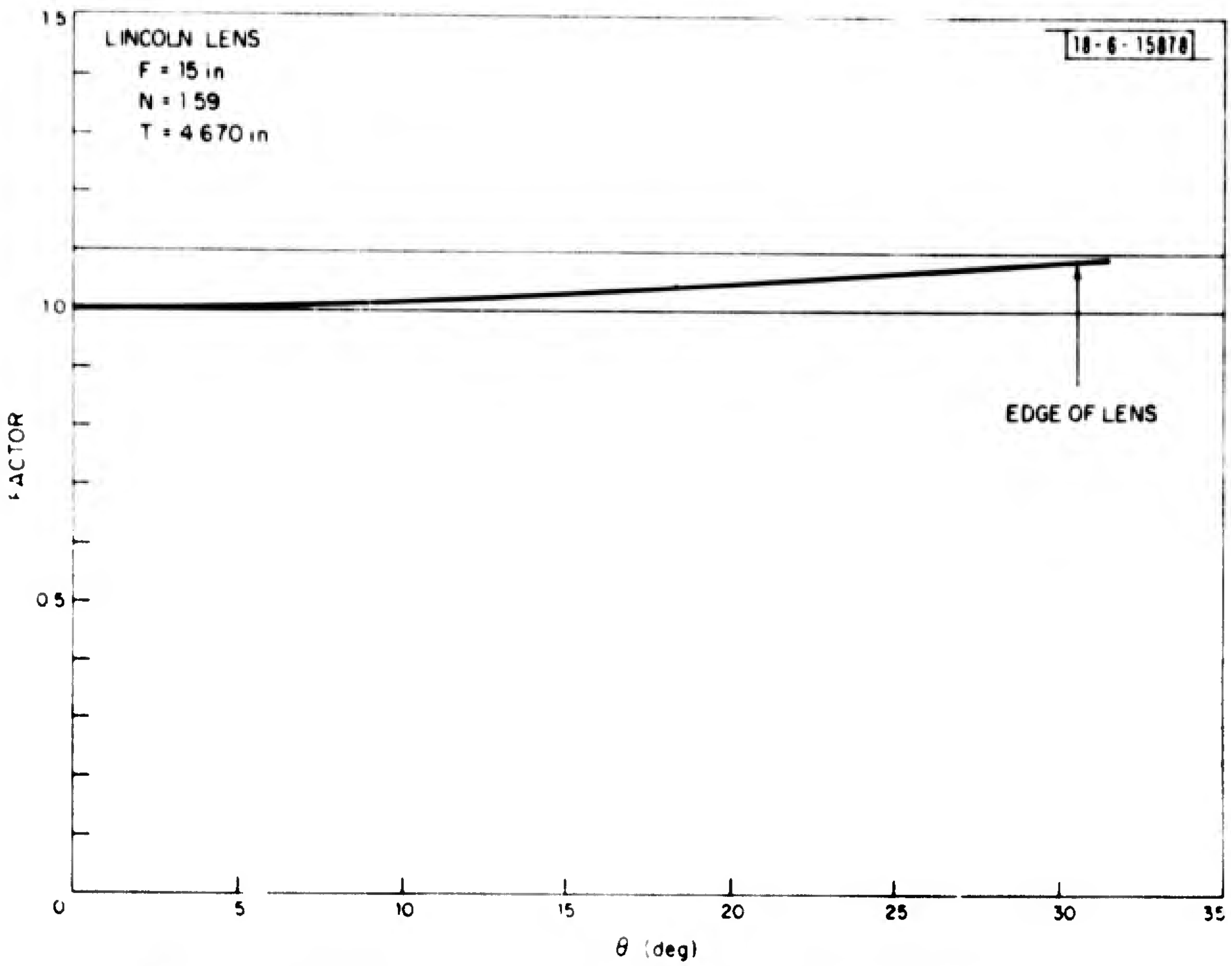

Fig. I-3. Modification of aperture distribution due to lens.

Appendix II

The Radiation Pattern of a Circularly Symmetric Aperture Enclosed in a Homogeneous Spherical Radome

Consider the geometry illustrated in Fig. (16). The following analysis for the radiation pattern is based on the applicability of geometrical optics, in which we assume that the exit rays from the circular aperture propagate in straight lines to the radome. The rays are then transformed through the radome using the transmission coefficients for a plane wave incident an an angle γ on a locally planar dielectric slab of thickness t. The rays then exit the radome along the same direction as the incident ramp (valid if $t/R \ll 1$), i.e., parallel to the z-axis, slightly displaced vertically, as indicated in the figure. The transmission of the rays through the radome is a strong function of the polarization of the wave relative to the plane of incidence, which is defined as the plane containing the normal to the surface and the direction of incidence. If we assume the incident polarization is in the x-direction, we observe from Fig. II-1 that the field separates into two orthogonal components: $E^{\parallel}$, which is parallel to the plane of incidence, and $E^{\perp}$, which is perpendicular to the plane of incidence. Thus in terms of the cylindrical coordinates (ρ, ϕ, z) the exit field over the aperture just outside the radome takes the form

$$\underline{E}_a = E_o(\rho)\cos\phi\, T^{\parallel}(\Psi)\, e^{-j\Phi(\Psi)}\hat{\rho}$$

$$- E_o(\rho)\sin\phi\, T^{\perp}(\Psi) e^{-j\Phi(\Psi)}\hat{\phi} \qquad \text{(II-1)}$$

where $T^{\parallel}(\Psi)$ is the transmission coefficient for plane wave incident on a dielectric slab of thickness t at an angle of incidence Ψ, and similarly for $T^{\perp}(\Psi)$, the transmission coefficient for waves normally polarized to the plane of incidence. The effective phase shift, $\Phi(\Psi)$, accounting for propagation through the radome, is easily shown to be

$$\Phi(\Psi) = k_o t\cos\Psi \qquad \text{(II-2)}$$

The angle Ψ is related to the aperture coordinate ρ via the relation

$$\rho = (R + t)\sin\Psi \qquad \text{(II-3)}$$

The transmission coefficients $T^{\parallel}(\Psi)$ and $T^{\perp}(\Psi)$ are given in Appendix III, i.e., Eq. (III-1) thru Eq. (III-4), with θ replaced by Ψ. For the lens antenna, the incident field $E_o(\rho)$ is readily determined from the primary feed pattern as follows: The distribution inside the radome is given by $E_o(x)$, where

$$x = F\tan\gamma = R\sin\Psi$$

$E_o(x)$ is thus readily obtained from the feed pattern which is measured as a function of γ. After ray tracing through the radome, the ray emanates at slightly increased height ρ, given by

$$\rho = (R + t) \sin\Psi = \left(\frac{R+t}{R}\right) x$$

$E_o(x)$ then becomes $E_o(\rho)$ outside the radome, and is modified by the proper transmission coefficients and phase delay as indicated in (II-1) to give the aperture distribution.

It is convenient to rewrite Eq. (II-1) in the abreviated form

$$\underline{E}_a(\rho, \phi) = E_\rho(\rho)\cos\phi\,\hat{\rho} - E_\phi(\rho)\sin\phi\,\hat{\phi} \qquad \text{(II-4)}$$

where

$$E_\rho(\rho) = E_o(\rho) T^{\parallel}(\Psi) e^{-j\Phi(\Psi)} \qquad \text{(II-5)}$$

$$E_\phi(\rho) = E_o(\rho) T^{\perp}(\Psi) e^{-j\Phi(\Psi)} \qquad \text{(II-6)}$$

where Ψ is assumed a function of ρ by virtue of Eq. (II-3). The far-field pattern can then be determined from the Fourier transform of the aperture distribution,

$$\underline{N} = \iint_A \underline{E}_a(\rho', \phi') e^{+jkx'\sin\theta\cos\phi} e^{+jky'\sin\theta\sin\phi} dz' dy' \qquad \text{(II-7)}$$

where A represents the area of the circular aperture. The far-field components E_θ, E_ϕ are then given by[5]

$$E_\theta = \frac{jke^{-jkr}}{4\pi r} (1 + \cos\theta) \left[N_x \cos\phi + N_y \sin\phi\right] \qquad \text{(II-8)}$$

$$E_\phi = \frac{-jke^{-jkn}}{4\pi n} (1 + \cos\theta) \left[N_x \sin\phi - N_y \cos\phi\right] \tag{II-9}$$

The components N_x are readily determined if we utilize the unit vector transformation

$$\hat{\rho} = \hat{x}\cos\phi + \hat{y}\sin\phi \tag{II-10}$$

$$\hat{\phi} = -\sin\phi\hat{x} + \cos\phi\hat{y} \tag{II-11}$$

Then, after some combination of terms, and transforming x', y' to cylindrical coordinates (ρ', ϕ'), we obtain

$$N_x = \frac{1}{2} \int_0^{2\pi}\int_0^a \rho' d\phi' d\rho' \left[E_\rho(\rho') + E_\phi(\rho')\right] e^{+jk\rho'\sin\theta\cos(\phi-\phi')} \tag{II-12}$$

$$+ \frac{1}{2} \int_0^{2\pi}\int_0^a \rho' d\phi' d\rho' \cos 2\phi' \left[E_\rho(\rho') - E_\phi(\rho')\right] e^{+jk\rho'\sin\theta\cos(\phi-\phi')}$$

and

$$N_y = \int_0^{2\pi}\int_0^a \rho' d\phi' d\rho' \cos\phi' \sin\phi' \left[E_\rho(\rho') - E_\phi(\rho')\right] e^{+jk\rho'\sin\theta\cos(\phi-\phi')} \tag{II-13}$$

The integration on ϕ' can be performed using the identity[5]

$$e^{+j\alpha\cos(\phi-\phi')} = \sum_{n=-\infty}^{\infty} (j)^n J_n(\alpha)\, e^{+jn\phi}\, e^{-jn\phi'} \tag{II-14}$$

where $J_n(\alpha)$ is the conventional Bessel function of order n and argument α. Using (II-14) in (II-13), we obtain, after simplification

$$N_x = \pi(F_{0\rho} + F_{0\phi}) - \pi\cos 2\phi \left[F_{2\rho} - F_{2\phi}\right] \tag{II-15}$$

$$N_y = \pi\sin 2\phi \left[F_{2\phi} - F_{2\rho}\right] \tag{II-16}$$

where we have defined

$$F_{0\rho}(\theta) = \int_0^a J_o(k\rho'\sin\theta)\, E_\rho(\rho')\rho'\, d\rho' \tag{II-17}$$

$$F_{0\phi}(\theta) = \int_0^a J_o(k\rho'\sin\theta)\, E_\phi(\rho')\rho' d\rho' \tag{II-18}$$

$$F_{2\rho}(\theta) = \int_0^a J_2(k\rho'\sin\theta)\, E_\rho(\rho')\rho' d\rho' \tag{II-19}$$

and

$$F_{2\phi}(\theta) = \int_0^a J_2(k\rho'\sin\theta)\, E_\phi(\rho')\rho' d\rho' \tag{II-20}$$

Substituting (II-15) and (II-16) into the expressions for E_θ and E_ϕ, we finally obtain, after considerable manipulation

$$E_\theta = \frac{jke^{-jkr}}{4r}(1+\cos\theta)\cos\phi\left[(F_{0\rho} + F_{0\phi}) + (F_{2\phi} - F_{2\phi})\right] \quad \text{(II-21)}$$

$$E_\phi = \frac{-jke^{-jkr}}{4r}(1+\cos\theta)\sin\phi\left[(F_{0\rho} + F_{0\phi}) - (F_{2\phi} - F_{2\rho})\right] \quad \text{(II-22)}$$

The two principal plane patterns are then readily determined. For the E-plane pattern ($\phi = 0$): $E_\phi = 0$),

$$E_\theta = \frac{-jke^{-jkr}}{4r}(1+\cos\theta)\left[(F_{0\rho} + F_{0\phi}) + (F_{2\phi} - F_{2\rho})\right] \quad \text{(II-23)}$$

For the H-plane pattern ($\phi = \pi/2$): $E_\theta = 0$,

$$E_\phi = \frac{-jke^{-jkr}}{4r}(1+\cos\theta)\left[(F_{0\rho} + F_{0\phi}) - (F_{2\phi} - F_{2\phi})\right] \quad \text{(II-24)}$$

Hence, due to the radome, the two principal plane patterns will no longer be identical.

Cross-Polarization Component

The comparison of the measured and calculated cross-polarized far-field patterns necessitates that the two respective coordinate systems be related. This is illustrated in Fig. II-2 where the measured system is denoted by (x',y',z') and the system used for calculations by (x,y,x). We define the dominant polarization according to

$$DP \equiv \text{DOMINANT POLARIZATION} = \hat{\theta}' \cdot \underline{E} \quad \text{(II-25)}$$

$$CP \equiv \text{CROSS POLARIZATION} = \hat{\phi}' \cdot \underline{E} \quad \text{(II-26)}$$

It thus remains to express DP and CP in terms of (r, θ, ϕ) and $(\hat{\theta}$ and $\hat{\phi})$.

To accomplish this, consider the expressions for the two radial unit vectors in in each system:

$$\hat{r} = \sin\theta\cos\phi\hat{x} + \sin\theta\sin\phi\hat{y} + \hat{z}\cos\theta \qquad \text{(II-27)}$$

$$\hat{r}' = \sin\theta'\cos\phi'\hat{x}' + \sin\theta'\sin\phi'\hat{y}' + \hat{z}'\cos\theta' \qquad \text{(II-28)}$$

However $r = r'$ and from Fig. II-2, $\hat{x} = \hat{z}'$, $\hat{y} = \hat{x}$, $\hat{z} = \hat{y}$.' Equating the respective components, then, we obtain

$$\sin\theta\cos\phi = \cos\theta' \qquad \text{(II-29)}$$

$$\sin\theta\sin\phi = \sin\theta'\cos\phi' \qquad \text{(II-30)}$$

$$\cos\theta = \sin\theta'\sin\phi' \qquad \text{(II-31)}$$

Alternately, using (II-30) and (II-31)

$$\tan\phi' = \mathrm{ctn}\theta/\sin\phi \qquad \text{(II-32)}$$

Using the technique employed in Ref. 6, we equate the gradients in each system, i. e.,

$$\nabla'(\cos\theta') = \nabla(\sin\theta\cos\phi) \qquad \text{(II-33)}$$

$$\nabla'(\tan\phi') = \nabla(\mathrm{ctn}\theta/\sin\phi) \qquad \text{(II-34)}$$

Equation (II-33) then leads to

$$\hat{\theta}' = -\frac{\cos\theta\cos\phi}{\sqrt{1-\sin^2\theta\cos^2\phi}}\,\hat{\theta} + \frac{\sin\phi}{\sqrt{1-\sin^2\theta\cos^2\phi}}\,\hat{\phi} \qquad \text{(II-35)}$$

and Eq. (II-34) leads to

$$\hat{\phi}' = \frac{-\sin\phi}{\sqrt{1-\sin^2\theta\cos^2\phi}}\,\hat{\theta} - \frac{\cos\theta\cos\phi}{\sqrt{1-\sin^2\theta\cos^2\phi}}\,\hat{\phi} \qquad \text{(II-36)}$$

Thus the expressions for the measured dominant and cross-polarized components of the radiation pattern can now be expressed in terms of the computed fields $E_\theta(\theta, \phi)$, $E_\phi(\theta, \phi)$ using (II-25) and (II-26):

$$DP = \frac{-\cos\theta\cos\phi}{\sqrt{1-\sin^2\theta\cos^2\phi}}\,E_\theta + \frac{\sin\phi}{\sqrt{1-\sin^2\theta\cos^2\phi}}\,E_\phi \qquad \text{(II-37)}$$

$$CP = \frac{-\sin\phi E_\theta}{\sqrt{1-\sin^2\theta\cos^2\phi}} - \frac{\cos\theta\cos\phi}{\sqrt{1-\sin^2\theta\cos^2\phi}}\,E_\phi \qquad \text{(II-38)}$$

We observe that CP = 0 along the two principal planes, $\phi = 0$ and $\phi = \pi/2$ as expected. The cross-polarized term is maximum in the plane $\phi = \pi/4$, as can readily be seen using (II-21) and (II-23) in (II-38), and noting that the maximum of $\sin\phi\cos\phi$ occurs at $\phi = \pi/4$.

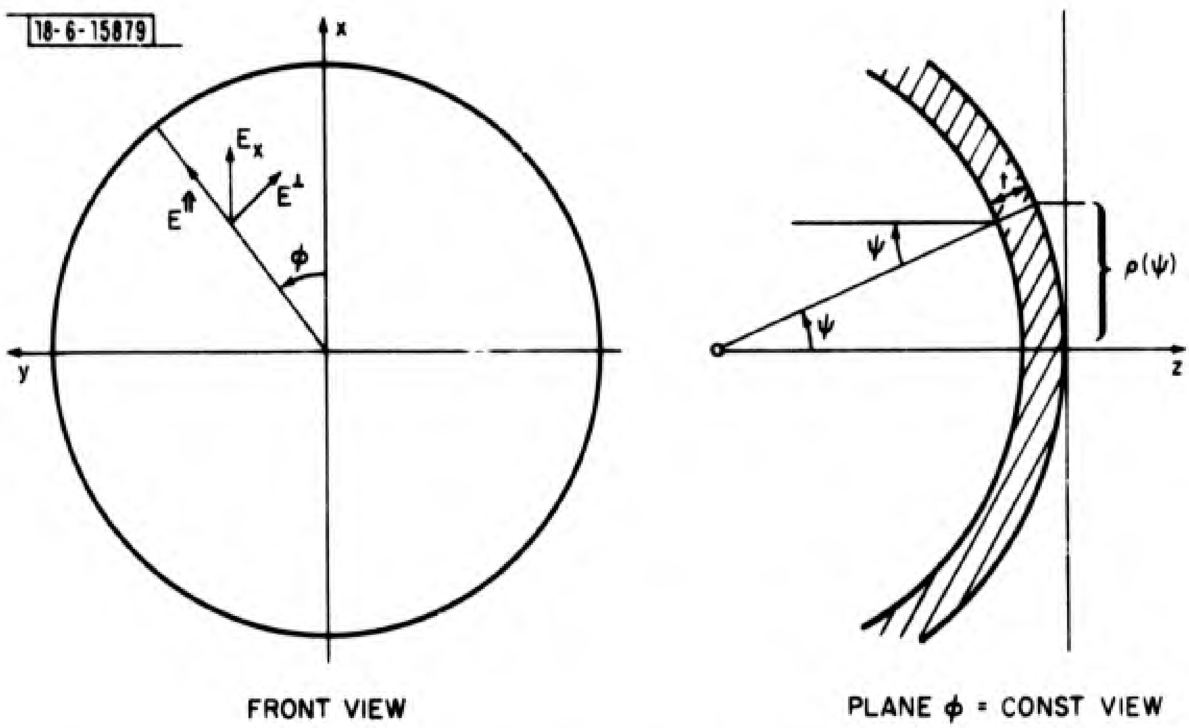

Fig. II-1. Transit of the incident polarization through the radome.

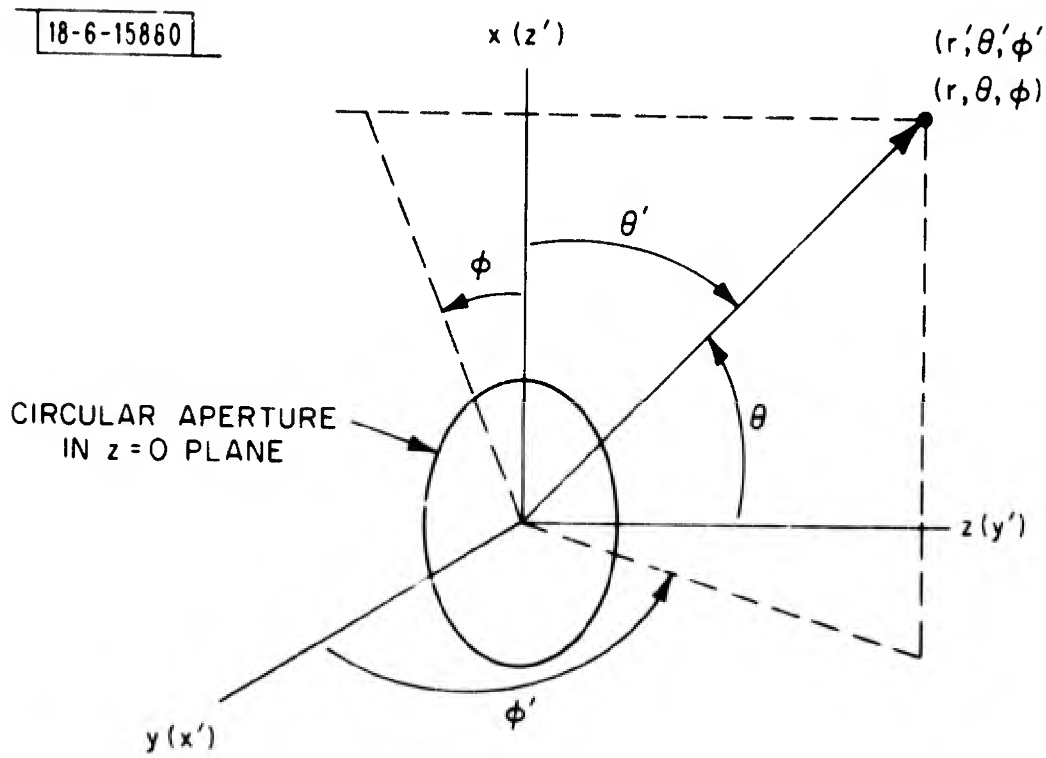

Fig. II-2 Measured (n', o', φ') and calculated (n, o, φ) coordinate systems.

Appendix III

Transmission Through a Spherical Radome, Geometric Optics Approach

The total loss of power due to the radome may be approximately estimated by adding up the loss of energy associated with each ray leaving the aperture of the antenna and striking the radome. Because of the curvature of the radome, the rays strike at various angles of incidence, and thus have different transmission coefficients. The basic formulas used are those for plane waves incident on flat homogeneous dielectric sheets--it is assumed that locally the radome acts like a plane sheet, an approximation that should be valid if the radius of curvature is large compared to the wavelength. The formula used[7] applies for the low-loss case: $(\tan\delta << 1)$.

$$T = \frac{F_b(1-r^2)}{1-F_b^2 r^2} \tag{III-1}$$

Two cases must be distinguished, that for the electric field polarized parallel to and normal to the plane of incidence. For the former,

$$r = r_p = \frac{\sqrt{\varepsilon_c - \sin^2\theta} - \varepsilon_c \cos\theta}{\sqrt{\varepsilon_c - \sin^2\theta} + \varepsilon_c \cos\theta} \quad \text{(parallel)} \tag{III-2}$$

and for the latter,

$$r = r_N = \frac{\cos\theta - \sqrt{\varepsilon_c - \sin^2\theta}}{\cos\theta + \sqrt{\varepsilon_c - \sin^2\theta}} \quad \text{(normal)} \tag{III-3}$$

Also

$$F_b = e^{-j\left(2\pi d\sqrt{\varepsilon_c - \sin^2\theta}/\lambda_o\right)} \tag{III-4}$$

where

$$\varepsilon_c = \frac{\varepsilon'}{\varepsilon_o}(1 - j\tan\delta)$$

θ = angle of incidence

d = thickness of dielectric sheet

We now consider a plane circular aperture inside a spherical radome of radius R, with its axis along a diameter of the radome. The rays from the aperture are assumed to be collimated into a parallel beam and strike the radome at angles of incidence θ, where $R\sin\theta$ is the distance ρ of the aperture point from the axis of the aperture as shown in Fig. (III-1). For convenience, we assume the amplitude distribution in the aperture is circularly symmetric and may be expressed as a function of θ, $F(\theta)$. The aperture field is also assumed to be polarized in the x-direction, so the parallel polarization component of the general ray striking the radome is proportional the $\cos\phi$, and the normal polarization component proportional to $\sin\phi$, where

ϕ is the azimuthal coordinate measured from the x-axis, in the x-y plane. In the absence of the radome, the peak gain would be proportional to

$$G_o \sim \left[2\pi \int_0^{\theta_{max}} F(\theta)\sin\theta d\theta \right]^2 \tag{III-5}$$

In the presence of the radome, the peak gain for the wave polarized in the x-direction is

$$G \sim \left[\int_0^{2\pi} \int_0^{\theta_{max}} F(\theta)\sin\theta \left[T_p(\theta)\cos^2\phi + T_N(\theta)\sin^2\phi \right] d\theta d\phi \right]^2 \tag{III-6}$$

The ϕ- dependence may be integrated directly so that

$$\frac{G}{G_o} = \left[\frac{\int_0^{\theta_{max}} F(\theta)\sin\theta \frac{T_p(\theta) + T_N(\theta)}{2} d\theta}{\int_0^{\theta_{max}} F(\theta)\sin\theta d\theta} \right]^2 \tag{III-7}$$

The transmission loss through a flat homogeneous dielectric panel is minimized when the thickness is a multiple of a half-wavelength in the dielectric medium. For the curved radome, an optimum thickness for any given frequency is also obtained, although the variation in transmission loss with thickness is less than for the flat plate, because the optimum thickness varies with incidence angle. Thus even for a lossless dielectric, zero reflection cannot be achieved with a uniform radome thickness because the optimum thickness is a function of angle of incidence and of frequency. Figure III-2 shows a typical calculation of the transmission loss (i. e., G/G_o in dB) for a spherical radome vs radome thickness at a frequency of 37 GHz. The material was assumed to have $\varepsilon'/\varepsilon_o = 4.5$, $\tan\delta = 0.01$, typical of Pyrex glass. For convenience in integration, the amplitude taper was assumed to be $f(\theta) = \cos^6\theta$, with $\theta_{max} = 45°$, corresponding to an 18-dB edge taper, typical of what might be expected from a low sidelobe antenna design. This value of θ_{max} corresponds to an 18-inch antenna inside a radome of inner diameter 25.5 inches. The arrows on the curve indicate the thickness for maximum transmission, assuming normal incidence on a planar dielectric having the same thickness as the radome, i.e., $d = n\lambda/(2\sqrt{\varepsilon_R})$, where n is an integer. Thus optimizing thickness, including the effect of the curvature of the radome, yields approximately .2 dB increase in gain.

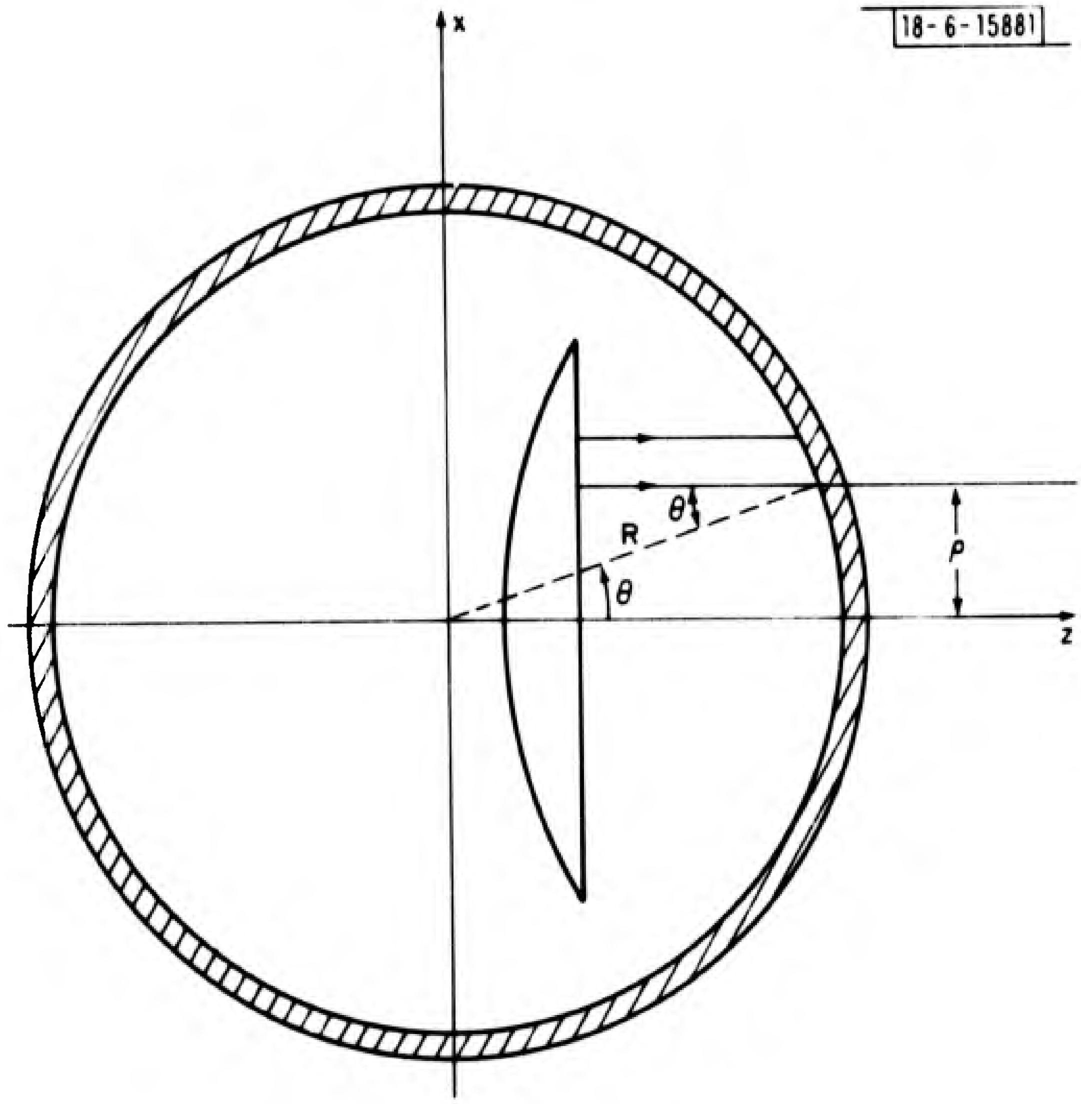

Fig. III-1. Plane Aperture inside spherical radome.

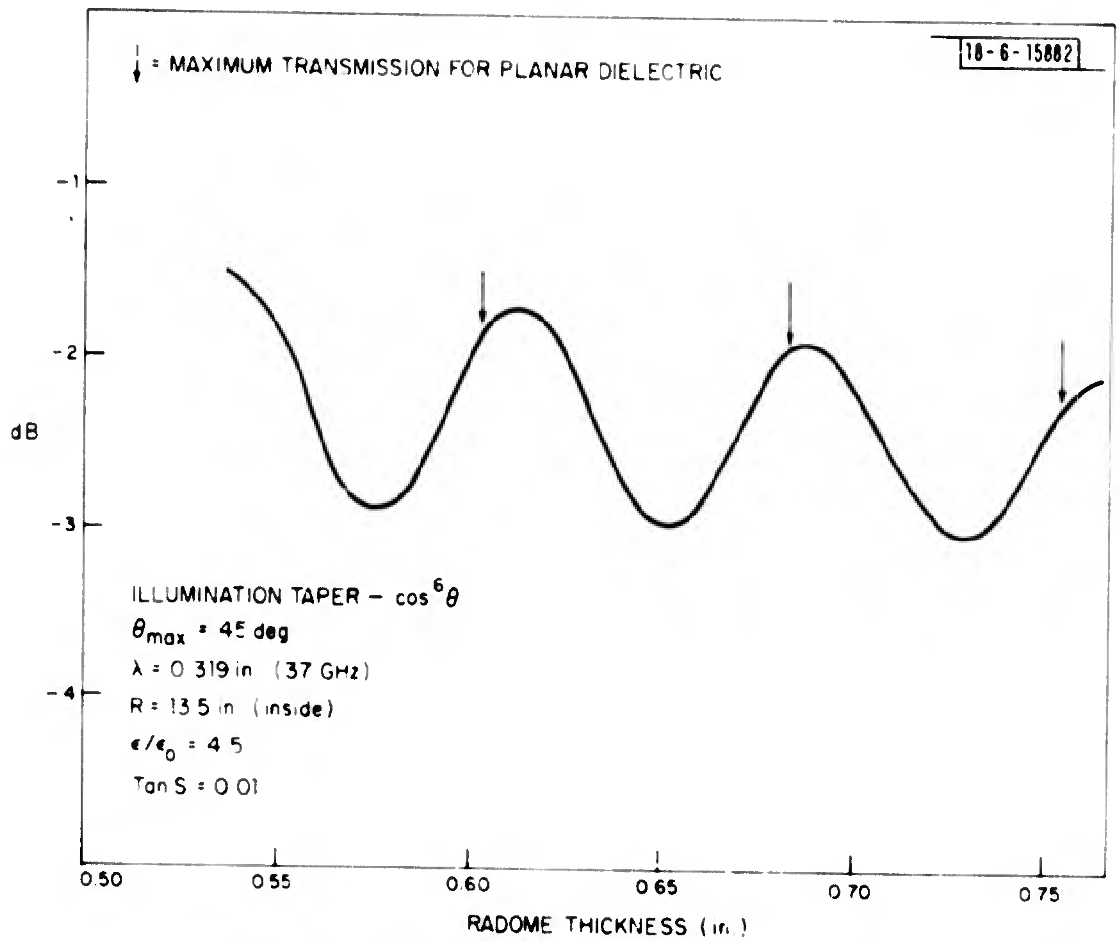

Fig. III-2. Transmission loss pyrex radome.

References

1. T. T. Taylor, "Design of Circular Apertures for Narrow Beamwidth and Low Sidelobes," Trans. IRE, PGAP AP-8, 17-22 (1960).

2. R. C. Hansen, Microwave Scanning Antennas, Vol. I (Academic Press, New York, 1964).

3. A. R. Dion, unpublished data on K_a-band Low-Sidelobe Axial Feed.

4. S. Silver, Microwave Antenna Theory and Design, Vol. 12 (McGraw-Hill, New York, 1949), Chap. 11.

5. Ibid., Chap. 6.

6. D. L. Sengupta, et al., "Azimuth and Elevation Direction Finder Study," The University of Michigan ECOM-01499-1 (December 1965).

7. W. M. Cady, M. B. Karelitz and L. A. Turner, Radar Scanners and Radomes Vol. 26 (McGraw-Hill, New York, 1948), pp. 266 and 354.